Computational and Experimental Investigation Towards a Stable Lithium Metal Anode

by

He Huang

A thesis

presented to the University of Waterloo

in fulfillment of the

thesis requirement for the degree of

Master of Science

in

Chemistry

Waterloo, Ontario, Canada, 2016

AUTHOR'S DECLARATION

This thesis consists of material all of which I authored or co-authored: see Statement of Contributions included in the thesis. This is a true copy of the thesis, including any required final revisions, as accepted by my examiners.

I understand that my thesis may be made electronically available to the public.

STATEMENT OF CONTRIBUTIONS

This work was the result of collaboration with Dr. Xiao Liang, with valuable help from Quanquan Pang and Xiaoqi Sun.

Abstract

Lithium metal is the ‘Holy Grail’ negative electrode of rechargeable batteries as it has the highest theoretical specific capacity and lowest electrochemical potential among all candidates. Next generation high capacity, high energy density battery systems, like lithium sulfur batteries, lithium air batteries, can never reach the level of commercialization without a safe and reliable lithium metal anode. Unfortunately, lithium metal cannot yet be safely implemented in commercial battery packs because of dendrite growth. Dendrite growth of these anode materials can cause short circuit within the battery, leading to dangerous fire and explosion in practical battery working conditions. In this work, through a combination of first principle computational calculations and experimental work, surface alloying lithium metal was found to be a promising approach to enable lithium metal to be directly employed as anode in future lithium metal batteries. The alloy-film protected lithium is effectively stabilized to electrodeposition over 700 cycles (1400 hours) of repeated plating/stripping at a practical current density of 2 mA cm^{-2}. Ultra-long cycling life was realized for a $Li_4Ti_5O_{12}$ electrode paired with such alloy-protected lithium metal negative electrodes. This work sheds light on a new and promising research field where the lithium metal can be stabilized by a surface layer/SEI with a low Li diffusion energy barrier.

Acknowledgements

I would like to express my thanks to my supervisor Professor Linda F. Nazar. I would also like to extend my gratitude to Dr. Xiao Liang, Quanquan Pang, Xiaoqi Sun and all other members in our group. On the other side, I would like to acknowledge SHARCNET, Compute Ontario and Compute/Calcul Canada for granting me access to the high performance computing platform (especially the CPU clusters Brown and Saw, and the GPU clusters Copper and Mosaic), for all those useful webinars on high performance computation on SHARCNET. Finally, I would like to express my gratitude to two SHARCNET consultants Jemmy Hu and Fei Mao. They helped us compiling VASP to run on SHARCNET. Fei Mao also helped us to take advantage of the high performance GPU clusters on SHARCNET. They also helped me on some technical issues when using SHARCNET for all the computation work. Without all the help, resources and/or financial support from you, this work cannot be done. Thank you all!

List of Figures

List of Tables

Chapter 1

Introduction and Background

1.1 Introduction

Since the major technical improvements on the efficiency of combustion engine, gasoline has been used to power the majority of the automobiles and vehicles on the planet and it drives the growth of global economy. This was all good until people gradually realized the negative environmental effect of burning gasoline or fossil fuels: it releases large amount of carbon dioxides and other harmful gaseous species into the atmosphere at an unprecedented and ever-increasing rate every year, leading to exacerbated global warming and environment pollution. With the increasing demand of energy globally, the price of fossil fuel is increasing, and it also affects the economy growth and national security of every country. Therefore, much effort has been spent on finding alternative environmentally friendly energy sources to reduce the reliance on fossil fuel and gasoline to power the economy. Hydropower, solar energy, wind energy, biomass, nuclear energy, geothermal energy and tidal energy, to name a few, have been intensively studied in the past decades to generate greener energy that release zero or much less carbon dioxides to the environment. One of the best ways to utilize those green energy is to transform them into electricity. The electricity that can be generated yearly from wind and solar are hundreds and thousands times bigger than the annual consumption of electricity in the world. But the sun is not shining in the night and the wind is not blowing every day. So any electricity generated has to be either consumed the next second by us or has to be stored in an energy storage system. Therefore, effective energy storage system is

the last key component to close the circle in order to take full advantage of all of those green technologies. Rechargeable batteries are one of the most popular energy storage systems to store excess electricity for future use. They store the energy in the form of chemical energy. When in demand for energy, the battery can release the energy in the form of electricity with high efficiency of conversion and zero release of greenhouse gas or other harmful gases to the environment.

Since the commercialization of the first lithium ion cell by Yoshino in Asahi Kasei Corporation in the 1990s[1], lithium ion batteries (LIBs) have been widely used in our daily life, powering a variety of devices including our smartphones, laptops, and electric vehicles. The widespread applications of the LIBs are not possible without the discovery and continuous research on lithium intercalation chemistry in many cathode and anode materials. A state-of-the-art LIB is generally made of a carbon-based anode (e.g. graphite), a transition metal oxide intercalation materials based cathode (e.g. LiCoO2), with a separator soaked with a lithium ion containing liquid electrolyte in between (**Figure 1**). The cell is normally in the discharge state, meaning the theoretical capacity of the cell is limited to the amount of electrochemically accessible lithium ions in the cathode. The capacity will be even lower when a lithium-containing solid electrolyte interphase (SEI) forms irreversibly on the anode.

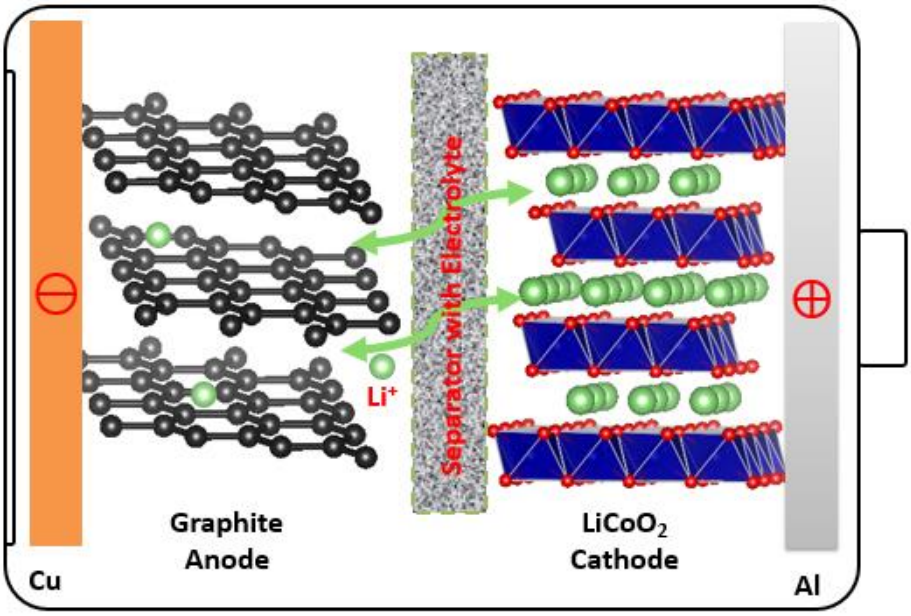

Figure 1. Illustration of the structure of a lithium ion battery with graphite as anode material on a Cu foil anode current collector, $LiCoO_2$ as cathode material on an Al foil cathode current collector, with a separator soaked with lithium ion conducting liquid electrolyte.

What's worse, with the increasing demands of portable electronic devices and electric vehicles, the limited energy density that can be provided by cathodes and anodes based on intercalation chemistry is not enough.[2] Alternative approaches based on conversion chemistry that promise higher energy densities have attracted increasing attention, such as Li/S, Li/O_2 batteries.[3] The advantages of these high energy systems are benefited from the combination of a very high capacity cathode and a lithium metal anode, which has a much higher specific capacity than graphite (3860 vs 370 mAh/g).[4] Although significant effort has been put into the cathode side of these systems, the success of any of these high capacity energy storage systems relies on the realization of a stable and safe Li-metal anode.

1.2 Towards a Stable Lithium Metal Anode

Various battery systems were compared in **Figure 2** with respect to the volumetric energy density and gravimetric energy density.[5] Even though lithium metal batteries offer the highest energy density (volumetric-wise and gravimetric-wise), it remains unsafe and not commercialized; one of the main reason is the inherent dendrite growth tendency of lithium metal during the charging process.[6] The growing of dendrites will induce further corrosion reaction with the electrolyte on prolonged cycling. The loss of available lithium source will result in capacity decaying, leading to a fading capacity. The worst issue of the dendrite growth of lithium metal anode is that it raises serious safety issues via cell short-circuit.[4]

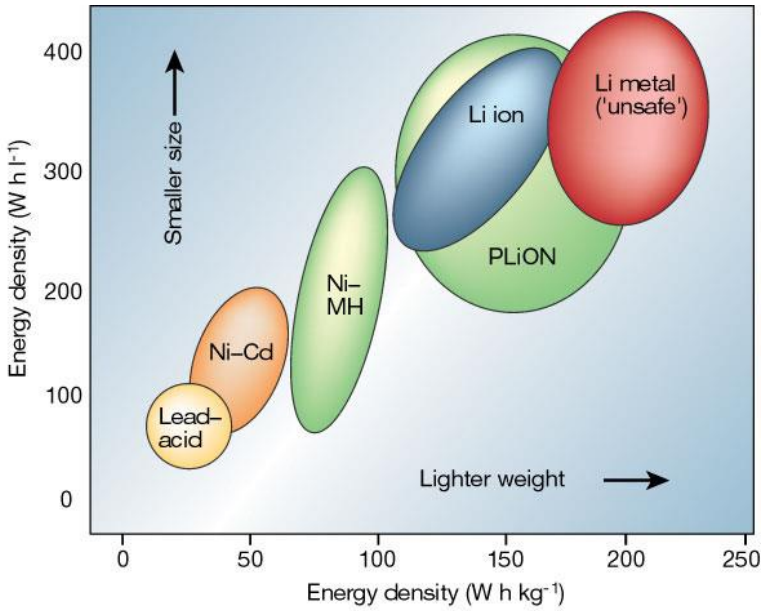

Figure 2. Different battery technologies with respect to volumetric energy density and gravimetric energy density.[5]

Continuous efforts have been made for decades to tackle the dendrite formation problem. Unfortunately, this problem is still pending for effective solutions, especially at a

practical current density of greater than 1 mA/cm^2. Different approaches, including in-situ generation of SEI on lithium anode by adding additives in the electrolyte[7–9], and ex-situ embellishment of lithium with artificial protection layer[10–12], or by pre-treatment methodology[13,14], have been reported to stabilize the lithium metal surface, and to achieve a uniform lithium electrodeposition. The electrolyte added with cesium ions was reported capable of eliminating dendrite growth at the nucleation step, because the cesium ion exhibits a lower reduction potential than the standard reduction potential of lithium ions and thus can create an electrostatic repulsive forces on the hot spots.[15] However, all these strategies were only effective for a few hundred cycles, and only at relatively low current density (typically less than 0.5 mA/cm^2) due to problems including low electron/ion conductivity and mechanical stability issues (e.g. cracks) of the protection layer. Depressing the dendrite formation by decreasing the actual current density via high surface area backbones/current collectors were reported recently[16,17], however, the plated lithium duplicate the porous structure and thus may suffer from severe corrosions with the electrolyte. Physically blocking the dendrite growth by solid electrolytes[18,19], and polymer electrolyte[20] with high shear modulus can, to some extent, prevent dendrite from crossing over to the cathode side. However, they do not change the fundamental, self-amplifying behavior of the dendrite growth.[3] Besides, application of these solid electrolytes are challenged by poor interface formed with both electrodes and their intrinsically low ionic conductivities at room temperature.[8] Though some sulfide solid electrolytes were reported recently to having

comparable ionic conductivity to that of liquid electrolytes, most of these systems are unfortunately not stable toward lithium metal.

Despite of tremendous number of models reported trying to explain the mechanism of the dendrite formation on lithium metal[21–23], these models are not able to address the puzzling fact that magnesium metal shows no tendency to have dendrite growth issue at the same plating/stripping condition[24]. And it is crucial to have a better understanding of surface growth behavior of those metals in order to prevent dendrite growth under different conditions.

Jäckle et al performed density functional theory (DFT) calculations and revealed the self-diffusion ability determines the different electrodeposition behaviors of lithium, sodium and magnesium.[25] Magnesium exhibits the preference to grow smooth surfaces as it has a low energy barrier (0.02 eV) of self-diffusion, while lithium and sodium are prone to nucleate dendrites because they have much higher diffusion barriers (0.14 and 0.16 eV, respectively). This theory is consistent with other calculations on electrolyte additives to suppress the dendrite growth, where it is reported that the activation energy barrier for lithium diffusion on the interface decreases by a value of 0.13 eV with the presence of fluoride anions.[26] Archer et al later delicately proved the theory by adding 30 mol% LiF in the simple liquid electrolyte (LiTFSI in PC), significant improvement in terms of lithium stability and dendrite suppression was achieved (but only at a relatively low current density of 0.38 mA/cm^2).[8] With the knowledge of achieving smooth lithium electrodeposition by

increasing the surface diffusivity, it opens up the chance to suppress the dendrite formation by tuning the lithium metal surface property.

1.3 First Principle Calculations

First principle DFT calculations have been adopted in numerous research on battery materials, including the excellent work on the study of dendritic growth of lithium and sodium and non-dendritic growth of magnesium.[25] Our work utilizes first principle calculations to search for promising candidates to prevent lithium metal anode from growing dendrite. First principle computational modeling has been adopted widely in the research community for battery materials. It can act as a complementary method to experimental techniques to either provide otherwise inaccessible evidence and insights to a complex material, or to speed up the discovery process and/or providing search direction for suitable battery materials.[27,28] High-throughput first-principle calculations were applied to systematically study various battery materials as well as all aspects of a battery material, including the voltage, capacity, ion mobility, chemical and thermal stability during charge and discharge.[29–31] Similar approach has also been adopted for fast screening for suitable materials for other energy storage systems, e.g. for methane storage[32].

Typically, first-principle calculations on solid materials involves many atoms, and they require huge computation resources that cannot be handled by a normal desktop computer or standalone workstations. These calculations are normally performed on supercomputer systems with hundreds and thousands of CPUs; some ab-initio software packages can even take advantage of graphic processing unit (GPU) to increase the speed of repetitive large-

scale mathematic operations. The calculations carried out in this work were done on CPU clusters including Brown and Saw, and on GPU clusters including Mosaic and Copper on the SHARCNET supercomputer platform.

Chapter 2

Theoretical Background

This work was done with the software package Vienna *Ab initio* Simulation Package (VASP)[33,34] taking advantage of the density functional theory (DFT) and the climbing image nudge elastic bands (CI-NEB) technique[35,36]. DFT calculations on VASP was used to provide ground state energy of each system. By comparing the energy difference of systems, we studied the structure, stability and adsorption properties of different materials. With the introduction of nudge elastic bands (NEB) technique to the DFT calculation, diffusion properties, including diffusion barrier, minimum energy paths (MEPs) on the surface of a system can be explored. With the advance of CI-NEB, an improved version of NEB, a precise transition state and the accurate activation energy barrier along a MEP can be obtained. The following explains the theoretical basis of these computational methods.

2.1 Density Functional Theory

When it comes to first-principle calculation or quantum chemistry, our first encounter, of course, is the non-relativistic time-independent Schrödinger equation (SE), the fundamental equation that describes the property of atoms and molecules. The SE has the following form:

$$\hat{H}\Psi = E\Psi \qquad 1$$

where $\hat{H}$ is the Hamiltonian operator describing a specific system, Ψ is the wavefunction, or a set of solutions or eigenstates of the Hamiltonian, and their corresponding eigenvalues, or the energy of the system, E. The Hamiltonian is composed of the following components:

$$\hat{H} = T_e(r) + T_N(R) + V_{eN}(r,R) + V_{NN}(R) + V_{ee}(r) \quad (2)$$

where **R** is the spatial coordinates of all nuclei in the system, and **r** is the spatial coordinates of all electrons. The first two terms are the kinetic energy of electrons and of nuclei in the system, the third term is the electron-nuclei attractive interaction term, the last two terms are columbic repulsion between electrons and between nuclei, respectively.

The SE that describes simple classical systems, such as particle in a box, harmonic oscillator, can be solved explicitly. But when faced with solid state materials, which involves many nuclei and many more electrons in the system, it will be practically impossible to find the exact analytical solutions to the SE of these many-body problems. DFT, however, is a successful method that can provide reasonable approximate solutions to the SE, and gives a reasonable prediction of the ground state energy and other properties of the system under study. The functioning of this method is based on a series of approximations.

2.1.1 Born-Oppenheimer approximation

Since electrons are massless in comparison with nuclei, electrons respond much more rapidly to the changes in their surroundings than nuclei do. Therefore, we can essentially separate the wavefunction into two components, one for describing nuclei and another for electrons. This is named the Born-Oppenheimer (BO) approximation.

$$\Psi(r,\mathrm{R}) = \Psi(\mathrm{r})\chi(\mathrm{R}) \quad (3)$$

where $\Psi(\mathbf{r})$ is the component corresponding to electrons, and $\chi(\mathbf{R})$ is for nuclei.

With this BO approximation, the problem can be solved in two steps computationally: First, the positions of all nuclei are fixed, electrons, being much lighter than the nuclei, in the

system will quickly respond and relax according to the movement of the nuclei. With this treatment, the second term in **Equation 2** can be removed and the fourth term turns into a constant, which therefore can be moved from the following Hamiltonian formulations and grouped with other constant terms. Then the SE can be rewritten as:

$$\hat{H}_e \Psi_e = E_e \Psi_e \quad 4$$

where $\hat{H}_e$ is the electronic Hamiltonian, Ψ_e is the electronic wavefunction, and E_e is the electronic energy. The electronic Hamiltonian $\hat{H}_e$ and the total energy E_{tot} are then

$$\hat{H}_e = T_e(\boldsymbol{r}) + V_{eN}(\boldsymbol{r}, \boldsymbol{R}) + V_{ee}(\boldsymbol{r}) \quad 5$$

$$E_{tot} = E_e + E_N \quad 6$$

where E_N is the constant nuclear repulsion term.

After the first step, the positions of the nuclei in the system can be updated iteratively, the program can go back to the first step, solve the SE in **Equation 4** and obtain the electronic energy E_e, calculate the nuclear repulsion term E_N, do a summation and obtain the total energy according to **Equation 6**. Therefore, the program produces a total energy of the system with each set of nuclei position input ($\boldsymbol{R}$). With the BO approximation, we can obtain a potential energy surface by solving for the electronic motion and nuclei motion separately.

2.1.2 Hartree-Fock approximation

In the **Equation 4**, we still need to solve the difficult problem of electronic wavefunction Ψ, which is a function of the coordinates of all electrons in the system $\boldsymbol{r}$. Hartree-Fock (HF) approximation is introduced to simplify the task. According to HF approximation, the

electronic wavefunction of a system with N electrons can be approximated as a product of N independent electronic wavefunctions:

$$\Psi = \Psi_1(r_1)\Psi_2(r_2)\cdots\Psi_{\mathrm{N}}(r_{\mathrm{N}}) \quad 7$$

With this approximation, the electronic wavefunction can be solved by solving for each individual wavefunction separately. However, there is a problem with this approximation: it does not conform to the Pauli exclusion principle. To fix this problem, the slater determinant was introduced. The slater determinant of a system with N electrons is a determinant of a N×N matrix of individual electron wavefunction in the following form:

$$\Psi(r_1, r_2, \cdots, r_N) = \frac{1}{\sqrt{N!}}\begin{vmatrix} \Psi_1(\boldsymbol{r}_1) & \Psi_2(\boldsymbol{r}_1) & \cdots & \Psi_N(\boldsymbol{r}_1) \\ \Psi_1(\boldsymbol{r}_2) & \Psi_2(\boldsymbol{r}_2) & \cdots & \Psi_N(\boldsymbol{r}_2) \\ \vdots & \vdots & \ddots & \vdots \\ \Psi_1(\boldsymbol{r}_N) & \Psi_2(\boldsymbol{r}_N) & \cdots & \Psi_N(\boldsymbol{r}_N) \end{vmatrix} \quad 8$$

2.1.3 Variational principle

When a system has an electronic wavefunction Ψ, the expectation value of the energy is:

$$E(\Psi) = \frac{\langle\Psi|\hat{H}|\Psi\rangle}{\langle\Psi|\Psi\rangle} \text{ where } \langle\Psi|\hat{H}|\Psi\rangle = \int \Psi^* \hat{H}\Psi d\boldsymbol{r} \quad 9$$

The variational principle states that the energy computed from a guessed wavefunction is an upper bound to the true ground-state energy. By minimizing the functional $E(\Psi)$ with respect to the N-electron wavefunction Ψ, we can obtain the ground state wavefunction Ψ_0 and the ground state energy $E_0 = E(\Psi_0)$.

2.1.4 Hohenberg-Kohn theorems and Kohn-Sham equations

With the BO approximation and HF approximation, the many-body problem with numerous dimensions is simplified to solving for a large number of individual electron wavefunctions. Yet it is still very complicate and computationally difficult to work with. Fortunately, Hohenberg and Kohn provided two theorems that greatly simplified the problem by taking advantage of the electron density. The electron density, $\rho(\boldsymbol{r})$, is the central quantity of DFT calculation. It is defined as a function of individual wavefunctions:

$$\rho(\boldsymbol{r}) = 2\sum_i \Psi_i^*(\boldsymbol{r})\Psi_i(\boldsymbol{i}) \qquad 10$$

Hohenberg and Kohn's first theorem states that the external potential for an interacting particle system is uniquely defined up to a constant by the ground state particle density $\rho_0(\boldsymbol{r})$. In other words, the ground-state electron density uniquely determines the energy, wave function and other properties of the system at ground state. This theorem is significant because it provides another possible approach to solve the SE by correlating the true electron density to the ground-state wavefunction of a system. It's especially important for large system like bulk solid state materials.

Hohenberg and Kohn's second theorem reveals that the functional that produces the ground state energy of the system will give the lowest energy if and only if the electron density is the true ground state electron density (This is similar to the variational principle). This means we can solve for the exact electron density if we can find the minimum of the energy functional. The ground-state energy functional with respect to the electron density is:

$$E(\rho) = T_e(\rho) + V_{ext}(\rho) + V_H(\rho) + E_{ex}(\rho) \quad 11$$

We have the exact expressions for all the terms on the right hand side that are known except for the exchange-correlation functional $E_{ex}(\rho)$. It represents the exchange and correlation interaction between electrons along with some other effects such as self-interaction correction terms.

The energy functional in **Equation 11** was used by Kohn-Sham to reformulate the SE in terms of the electron density:

$$\left[-\frac{\hbar^2}{2\mathrm{m}}\nabla^2 + V(\boldsymbol{r}) + e^2\int\frac{\rho(\boldsymbol{r}')}{|\boldsymbol{r}-\boldsymbol{r}'|}d^3\boldsymbol{r}' - V_{XC}(\boldsymbol{r})\right]\psi_i(\boldsymbol{r}) = \varepsilon_i\psi_i(\boldsymbol{r}) \quad 12$$

where the second term on the left side is the electron-nuclei attraction interaction, the third component is the interaction between an electron and the whole electron density of the system. The last component is the exchange-correlation potential:

$$V_{XC}(r) = \frac{\delta E_{XC}(r)}{\delta\rho(r)} \quad 13$$

The exchange-correlation potential is related to the exchange-correlation functional, $E_{XC}(\boldsymbol{r})$. But the exact form of this functional is not known. Finding the approximate form of the exchange-correlation functional has been the major challenge of DFT development. It has been approximated by several approaches. Two of the most popular approximations are the local density approximation (LDA) and the generalized gradient approximation (GGA). LDA defines the exchange-correlation functional by using the local density of the uniform electron gas, the exact form of which is known. In this system, electrons are balanced by a positive background charge distribution. The accuracy of LDA is generally not satisfactory to

describe the energetics of chemical reactions and activation energy barriers. However, LDA is the basis of all other approximate exchange-correlation functionals; for example, GGA takes one step further. It takes into account of not only the density $\rho(\boldsymbol{r})$, but also the gradient of the charge density at that specific point, $\nabla\rho(\boldsymbol{r})$, to simulate the non-homogeneous distribution of electrons. Other more complex approximations, such as hybrid approximations, were also available. They can increase the accuracy by 3 to 5 folds, enough for many applications in chemistry.

The Kohn-Sham equations can be implemented in a program to be solved iteratively until a certain stopping criterions are satisfied and the ground state electron density, the wavefunction and the ground state energy of the system are determined.

2.1.5 Plan-wave periodic systems

For solid state system, the material is generally crystalline. It can be described by a small unit cell with very few atoms, and by repeating the unit cell in all 3 dimensions in space, the bulk properties of the material can be reconstructed. By calculating on a small unit cell with limited amount of atoms, solid state materials with infinite number of atoms can be simulated efficiently with great accuracy in terms of their physical, chemical and other properties. When studying this type of periodic systems, the solution of SE must satisfy the Bloch theorem. The Bloch theorem states that the electron wavefunction will adopt the following form in periodic systems such as solid crystalline materials:

$$\psi_{\mathbf{k}}(\boldsymbol{r}) = \exp(i\mathbf{k}\cdot\mathbf{r})\, u_{\mathbf{k}}(\boldsymbol{r}) \qquad 14$$

where **k** vector is the wavevector in the reciprocal space, $u_{\mathbf{k}}(\boldsymbol{r})$ is a periodic function having the same periodicity as that of the crystal. This means that SE can be solved for each value of k independently, and mostly it is faster to solve SE in the reciprocal space. The exponential term in the right hand side describes a typical plane wave function; therefore, those calculations are referred to as plane wave calculations. In principle, integration over all possible k values is needed to construct the electron density. But fortunately the wavefunctions change slowly while changing the k value. Therefore, the selection of suitable k-point grids across the primitive cell in the reciprocal space (also called the first Brillouin Zone) is important in DFT calculations to generate converged result while not wasting computing resources.

The second part of **Equation 14** can be expanded in to a Fourier series:

$$u_{\mathrm{k}}(r) = \sum_G c_G \exp(iG \cdot r) \qquad 15$$

where $\boldsymbol{G}$ are the reciprocal lattice vectors, c_G are the Fourier coefficients. Combining **Equation 14** and **15**, we arrive at:

$$\psi_{\mathbf{k}}(\boldsymbol{r}) = \sum_{\mathrm{G}} c_{\boldsymbol{G}+\boldsymbol{k}} \exp(i(\boldsymbol{k}+\boldsymbol{G})\boldsymbol{r}) \qquad 16$$

The Fourier series is an infinite sum over all **G** vector values. But the functions are the solutions of the SE involving kinetic energy, which is $\frac{\hbar}{2m}|\boldsymbol{k}+\boldsymbol{G}|^2$. Therefore, the lower energy solutions are more significant in reality, we can ignore those high energy solutions. So a cutoff energy is generally introduced to truncate solutions with high kinetic energies. This is an important parameter that can affect the accuracy and speed of a DFT calculation. A

high cutoff energy will give more accurate results, but maybe much more computationally expensive. So the selection of the cutoff energy is another convergence test to make when performing DFT calculations to ensure the accuracy of the calculations.

2.1.6 Pseudopotentials

The core electrons in the DFT calculations can be approximated by pseudopotentials. There are several reason for it. Firstly, the core electrons are not important in many chemical reactions and physical processes. Mostly, only valence electrons are involved in determining the many properties of a system. Secondly, the core electrons are tightly bonded to the nucleus. It requires very high cutoff energy to include all electrons in the system into DFT calculations.

The high energy core electrons can be substituted by the frozen core approach where the electron density of core electrons is replaced by an effective density. The pseudopotential approach enables the use of much lower energy cutoff as well as less electrons for solving the SE.

Two types of pseudopotentials commonly used are ultrasoft pseudopotentials (USPP) and projected augmented wave (PAW) pseudopotentials. The USPP contain more empirical parameters, while PAW pseudopotentials require higher energy cutoffs but offer more accurate results across different systems and setup. In this work, PAW pseudopotentials were used for all calculations.

2.2 Nudge Elastic Band Method

The majority of the software packages implemented with DFT, including the one used in this work, have been designed to find the minimal energy configuration of the system. However, when the interest is to find the transition state, the highest energy configuration of the system along a pathway (**Figure 3**), another method is needed to do this type of calculations. The nudge elastic band (NEB) calculation is a very effective method to find the minimum energy pathway (MEP) of two minima on a potential energy surface (PES).[37] In this work, climbing image NEB (CI-NEB) method was adopted to study the diffusion pathways between two stable adsorption sites, and the activation energy barrier related to the MEP. The following in this section presents an introduction to the normal NEB method and the CI-NEB method.

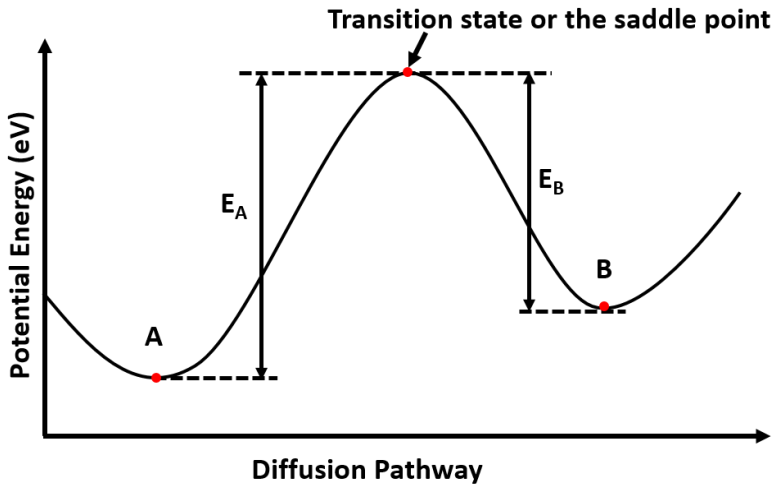

Figure 3. Schematic representation of surface diffusion in between stable site A and another stable site B along a minimum energy path on the potential energy surface, the activation energy barrier of the diffusion from site A is marked E_A, that of the diffusion from site B is marked E_B.

2.2.1 The normal NEB method

The NEB method starts with two minima, one being the initial state ($\boldsymbol{R_0}$), the other being the final state ($\boldsymbol{R_N}$). Then, several intermediate states or images ($\boldsymbol{R_1}, \boldsymbol{R_2}, \ldots, \boldsymbol{R_{N-1}}$) are created based on a specific technique, e.g. linear interpolation (**Figure 4**). The images are connected by imaginary springs with a spring constant *k*. The spring force on *i*th image is:

$$F_i^S|_{||} = k(|R_{i+1} - R_i| - |R_i - R_{i-1}|)\tau_i \qquad 17$$

where $\boldsymbol{\tau}_i$ is the normalized vector which is parallel to the local path of image ***i***.

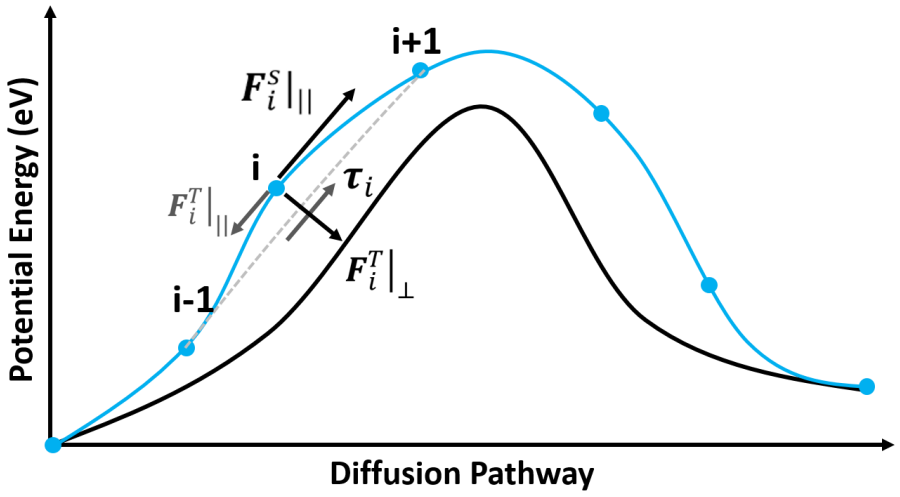

Figure 4. Illustration of the working principle of a typical nudge elastic band calculation for diffusion from one site to another. Each dot is one intermediate image interpolated in between the initial state and the final state. Forces are either perpendicular to the local tangent of the path, or parallel to it. F_i^S is the artificially added spring force, F_i^T is the true force. || or ⊥ subscript refers to the force component that are parallel or perpendicular to the local tangent of the path, τ_i.

The imaginary springs force the images to maintain their distance with each other. The energy of the interpolated images was minimized by DFT calculations, but under constrains with NEB algorithms. During a NEB calculation, the total force acted on an image is the sum

of the spring force parallel to the local path and the perpendicular component of true force with respect to the local path:

$$F_i = F_i^s|_{||} - \nabla E(R_i)|_{\perp} \quad 18$$

where E is the energy of the system, which is a function of all the atomic coordinates, the true force of the image is:

$$\nabla E(R_i)|_{\perp} = \nabla E(R_i) - \nabla E(R_i) \cdot \tau_i \quad 19$$

The component of the potential force perpendicular to the path $\boldsymbol{F}_i^T\big|_{\perp}$ is the driving force to push, or nudge all images on the band towards the minimum energy path instead of the local or global minimal sites on the PES. The springs were the main constrain to keep equal distance between neighboring images and to prevent each image from sliding down the PES along the MEP. The component of the potential force that is parallel to the local path, $\boldsymbol{F}_i^T\big|_{||}$, is removed to prevent it from interfering with the spring force and dragging the images down along the slop of PES.

However, with this normal NEB method, it is hard to find the exact transition state and the accurate activation energy barrier related to it (as clearly indicated in **Figure 5**[35]). Since all intermediate images in between the initial state and the final state are kept equal in distance. One has to do many NEB calculations along the path to 'chase for' the transition state. Even you sample numerous intermediate images in between, it is still highly possible that the real transition state is not exactly one of the sampled image. However, an improved version of NEB method, CI-NEB can easily find the exact transition state and the accurate

activation energy barrier under the same condition. The next section present details on the theory behind the CI-NEB method.

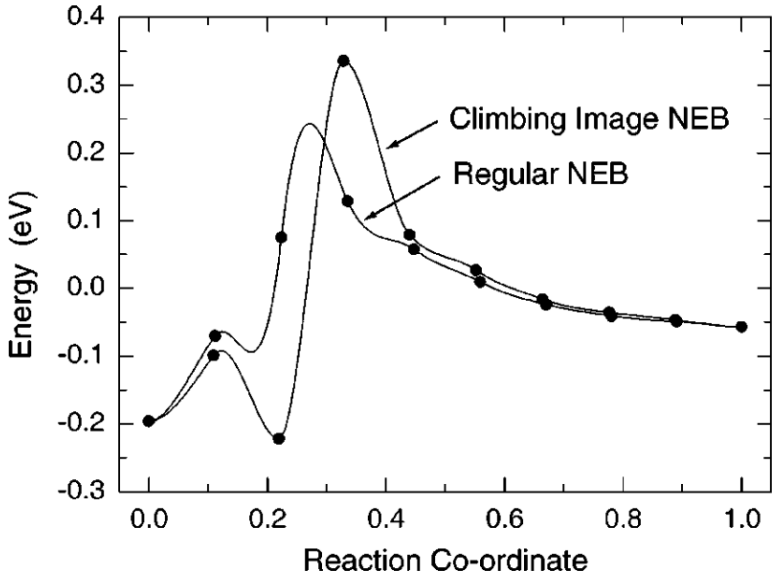

Figure 5. MEP for CH_4 dissociative adsorption on an Ir(111) surface calculated by regular NEB method and CI-NEB method.[35] The regular NEB did not find the transition state while CI-NEB found the exact transition state with the same number of images.

2.2.2 The climbing image NEB method

An improved version of NEB, the CI-NEB method will find out the exact transition state and activation energy barrier automatically.[35,36] In fact, the main difference between these two methods is only the slight modification on the force acted on the image with the highest energy after several iterations of calculation with the normal NEB method. The highest energy transition state is reached thanks to the removal of the spring force ($F_i^s|_{||}$ in **Figure 4**) on the image with the highest energy and inverting the component of the true force on this image that is parallel to the path ($F_i^T\big|_{||}$ in **Figure 4**) and apply onto the image. When the CI-

NEB mode is turned on, the total force experienced by the image with the maximum energy changed from **Equation 18** to the following:

$$F_{i_{max}} = -\nabla E\left(R_{i_{max}}\right) + 2\,\nabla E\left(R_{i_{max}}\right)\Big|_{||} \qquad 20$$

Therefore, instead of driving the structure into a local or global minimum, the inverted component of the true force drives this image up to the saddle point along the MEP, leading to obtaining the exact activation energy barrier(as clearly demonstrated in **Figure 5**[35]).

Chapter 3

DFT Calculations on Lithium Alloys

Since the surface diffusion energy barrier governs the Li growth behavior on the metal anode, dendrite formation can theoretically be suppressed by introducing a modified surface with a lower diffusion barrier. Surface alloying are known to change the surface properties of a metal. In this work, we carried out DFT calculations and CI-NEB calculations to search for lithium alloys with lower energy barriers for lithium diffusion on the surface. Protecting the lithium metal anode by these low-energy-barrier lithium-based alloys, it should be promising to synergistically resolve the surface chemical stability problem and dendrite issue of lithium metal anode.

3.1 Computational Details

The Vienna *Ab initio* Simulation Package (VASP)[33,34] was used to perform first principle DFT calculations on those alloys. The Perdew, Burke, and Ernzerhof (PBE) flavor of generalized gradient approximation (GGA)[38] was used to account for electronic exchange and correlation. We used projector augmented wave (PAW) pseudopotentials[39,40] with a cutoff energy of 400 eV in all calculations.

3.1.1 Bulk structure relaxation and optimization

For each system, bulk relaxation calculations were performed on $1 \times 1 \times 1$ unit cell. The k-point convergence test with respect to the energy for each system was done beforehand, and

suitable k-point grid were selected for each system. The quality of the calculations was verified by comparing the calculated lattice parameters with their experimental values.

3.1.2 Modeling the surface

The surface of a material was modeled by a slab of a supercell of 1×1 on the x and y direction, with 5 layers (6 layers for $Li_{13}In_3$ to ensure stoichiometry of the surface slab model is consistent with that of the bulk composition of the alloy) of surface atoms in thickness oriented parallel to z direction, with a large vacuum layer on top of the surface to avoid the interaction of the surface atoms of the slab with the surface atoms of its neighboring periodic slabs along the z direction.

The top 2 layers of the surface were allowed to fully relax along x, y and z directions to simulate the surface relaxation of a material, the middle layer were fully fixed to simulate the structure property of the bulk region of the material. The k-point convergence on the x and y direction for each slab is tested with respect to the slab energy. The k-point along z direction is set to 1 since the dimension along z is always much larger than that along x and y directions.

3.1.2.1 Surface energy

The stability of the surface can be characterized by its surface energy, E_s. Surface energy is the energy needed to cleave the bulk crystal along a specific surface. The most stable surface of a crystal has the lowest surface energy. The surface energy for alloys can be defined using the following equation:

$$E_s = \frac{1}{2A}\left(E_{slab} - n_{slab} \cdot \frac{E_{bulk}}{n_{bulk}}\right) \quad (21)$$

where $2A$ is the sum of the top and bottom surface area of the surface slab constructed, E_{slab} is the total energy of the slab from our DFT calculations, E_{bulk} is the energy of the bulk crystal from the bulk calculation described in the previous section, n_{slab} is the number of formula units in the surface slab supercell and n_{bulk} is the number of formula units in the unit cell of the bulk calculation. The surface with the lowest surface energy is most stable. Due to its relative stability, it represents a significant fraction of the total surface area of the crystal. Thus these surfaces are selected to represent the material.

3.1.3 Modeling lithium adsorption on the surface

Lithium adsorption on the stable surface of a material was modeled by adding a lithium atom on top of the fully relaxed surface slab of the material, similar to that from previous step. But for calculation of lithium adsorption and diffusion barriers, bigger slabs were made to minimize the interaction of lithium adatoms in adjacent supercells in x and y direction. In this work, the slabs were comprised of m × m supercell (m = 4 for Li, m = 2 for Li_3As, Li_3Bi and LiZn, m = 1 for $Li_{13}In_3$) with 5 layers of alloy atoms (6 layers for $Li_{13}In_3$ to ensure the stoichiometry of the slab was consistent with the bulk composition of the alloy) and a large enough vacuum layer. Similarly, the k-point convergence on the x and y direction for each slab was tested with respect to the slab energy. The k-point along z direction is set to 1 since the dimension along z is always much larger than that along x and y directions.

3.1.3.1 Adsorption energies

The surface growth behavior of a material is related to the energy gain or loss after adsorbing one atom onto the surface, which is the adsorption energy, E_{ads}.

$$E_{ads} = E_{a/s} - E_{slab} - E_{atom} \quad (22)$$

where $E_{a/s}$ is the energy of the surface slab with the adsorbed atom, E_{slab} the energy of the slab, and E_{atom} the energy of a single atom of the adsorbed species calculated from a supercell of the same size as that of the supercell of the slab.

Each surface has several potential sites where the new adsorbed atom would likely to sit on or diffuse across. And the lithium adsorption on the surface, or the potential energy surface (PES), can be well sampled by several high symmetry adsorption site. In this work, every high symmetry adsorption site on each surface was identified and calculated separately to determine if it is a stable adsorption site. The lithium adatom is positioned on every high symmetry site, and it is allowed to fully relax along with the top two layers of the surface slab. If the adatom stays at around its initial position, it is then determined to be a stable adsorption site, in another word, a global or local minimum on its PES.

3.1.4 Modeling lithium diffusion on the surface

Lithium adsorbed on the stable site can diffuse to the next stable site, but has to overcome a diffusion barrier. To calculate the diffusion barrier and determine the diffusion path, CI-NEB calculations were performed with VASP on those stable adsorption sites on the alloy surfaces.

The lower the different diffusion barrier, the easier an adsorbed lithium atom can move on the surface. Therefore, a lower diffusion barrier can facilitate a smoother electrodeposition and minimize dendrite growth.

3.2 Results and Discussion

3.2.1 Li metal

The diffusion of lithium on lithium metal was carried out in the beginning of this work. The result was compared with literature as a validation to our calculations. The diffusion barrier of lithium diffusion on lithium metal also serves as a reference to the rest of our calculations.

Lithium metal crystallizes in simple body-centered cubic (BCC) lattice (space group $Im\bar{3}m$). The structure was simulated based on the crystal structure data from Inorganic Crystal Structure Database (ICSD). The $1 \times 1 \times 1$ unit cell of lithium metal was used during bulk relaxation and optimization. The unit cell along with all atoms within were allowed to fully relax. After DFT calculations on the structure optimization and relaxation, the calculated unit cell parameter was in very good agreement with the experimental data[41] (**Table 1**) and the results in the literature[25].

Table 1. Unit cell parameters of Li from experiments and our DFT calculations

Li	**Exp. (Å)**	**Calc. (Å)**	**Δ** (%)
a/b/c	3.507[41]	3.443	1.819

The surface slab model of lithium metal was constructed based on the relaxed structure parameter of our calculation. Every crystalline material can have numerous surfaces exposed with different miller indices and/or terminations. Two surfaces with different miller indices and/or terminations can have very different compositions and/or arrangement of atoms on the surface and subsurface layers. Therefore, each surface can have a very different surface property. But the most stable surface will contribute more to the total surface area in reality. So the most stable surface of a material is normally selected as the representative surface for predicting its properties in DFT calculations.[25]

To find out the most stable surface of lithium metal, slabs were constructed to model each surface, and the calculated surface energies of low index surfaces, (001), (110) and (111), of lithium metal were collected in **Table 2**. They are in very good agreement with the literature value. The (001) surface of lithium metal has the lowest surface energy among the low index surfaces. The (111) surface has the highest surface energy. This order is typical in bcc packed structures.

Table 2. Calculated surface energies of low index surfaces of lithium metal from our DFT calculations compared with previous studies. [25,42]

E_S (J/m^2)	(001)	(110)	(111)
This work	0.448	0.490	0.534
Other works.	0.46[25], 0.47[42]	0.49[25], 0.50[42]	0.53[25], 0.56[42]

Since the (001) surface is the most stable surface of lithium metal, it will contribute more towards the total surface area of lithium metal anode. Therefore, this surface was selected to study the surface adsorption and diffusion property of lithium on lithium metal.

A larger surface slab was constructed for lithium adsorption and diffusion calculations in order to minimize interaction between two lithium adatom on neighboring supercell. The slab was constructed with 3×3 geometry of (001) surface, having 5-atomic-layer in thickness on z direction (**Figure 6**). To avoid the interaction of the surface atoms of the slab with the surface atoms of its neighboring periodic slabs along the z direction, a large vacuum layer was added on top of the surface slab. The top two layers of surface atoms were allowed to fully relax to simulate the surface relaxation on lithium (001) surface. The middle layer atoms were fixed to simulate the bulk structure of lithium metal. The slab was fully relaxed before a lithium atom is positioned on the surface to simulate lithium adsorption.

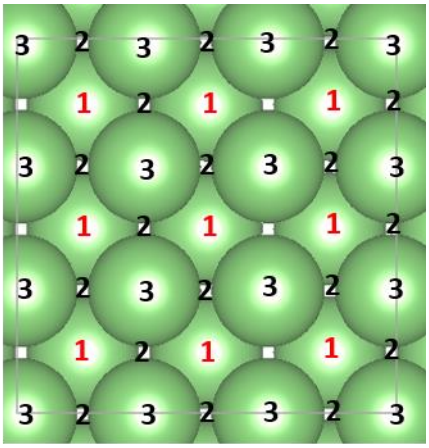

Figure 6. The lithium 3×3 geometry of (001) surface slab constructed, along with its high symmetry adsorption sites (numbered 1,2 and 3). The stable lithium adsorption sites (site 1) are colored red.

Due to the symmetry of examined surface, the potential energy surface (PES) of lithium adsorption on the surface and the activation energy barrier for the lithium adatom to diffuse across the surface can be well sampled representatively with a number of points. The adsorption of the lithium adatom on lithium metal was modeled by three characteristic high symmetry points (numbered 1, 2, 3 in **Figure 6**). After structure relaxation, only site 1 remained at its original place, while when the lithium adatom was originally positioned at site 2 or 3, it will spontaneously relax (diffuse) to site 1. Therefore, site 1 is determined to be the stable adsorption site with the lowest energy. This is also the global minimum on the PES of lithium adsorption on Li (100) surface. Li adatoms positioned on the other adsorption sites generate high energy state which are very unstable configuration, where the adsorbed lithium will spontaneously relax to the energy minimal stable site, site 1.

Lastly, the CI-NEB implemented in VASP was used to find the precise transition state (the highest energy saddle point), the minimum energy paths (MEP) and the diffusion barrier between two energy minima on the PES. According to our calculation, on the (100) surface of lithium metal, the lithium adatom hopping from one most stable adsorption site 1 to the next one has to go through a high energy transition state, site 2 (marked as 1→2→1 in **Figure 7a**). The energy difference between the global minimum site, site 1, and the transition state is 0.150 eV (**Figure 7b**), which is in very good agreement with the literature value.[25]

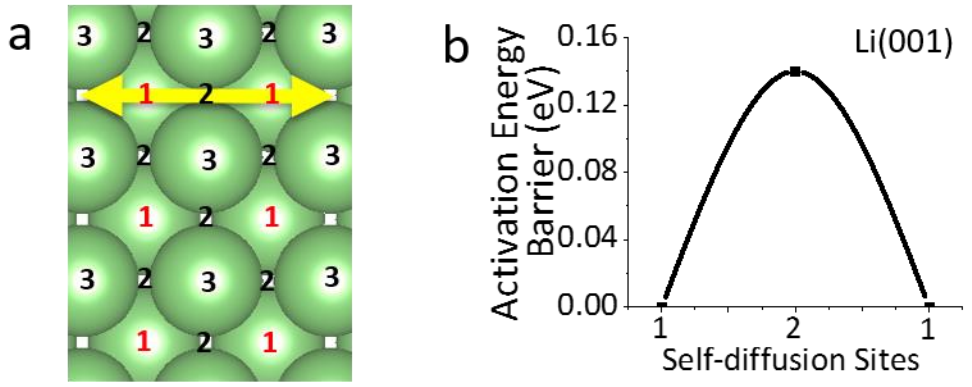

Figure 7. DFT calculations of the lithium diffusivity on the Li (001) surface. The (a) minimum energy paths between two neighboring stable adsorption sites (numbers colored red) and (b) their corresponding energy barrier calculated by climbing image nudge elastic band technique using VASP. The yellow arrow line in (a) indicate the existence of the long range MEP on the surface.

This means that a lithium adatom has to overcome a high energy barrier of 0.150 eV to be able to diffuse across the surface of lithium metal. This activation energy barrier is nearly 5 times of the intrinsic thermal energy at room temperature (0.026 eV). The activation energy and the thermal energy are related through the Arrhenius equation (Equation 23). Therefore, this equation can be used to qualitatively determine the likelihood of the surface diffusion process of lithium adatom on a surface.

$$k = A\mathrm{e}^{\frac{-E_{\mathrm{act}}}{k_{\mathrm{B}}T}} \qquad 23$$

where k represents the rate constant or likelihood of the occurrence of surface diffusion process of a lithium adatom from one stable adsorption site to the next one on the surface, A A is a pre-exponential factor, k_{B} is the Boltzmann constant, T is room temperature (as we are concerned with room-temperature LIBs in this work), and E_{act} is the activation energy of the elemental surface diffusion process under study. With an activation energy that is 5 times

larger than that of the room temperature thermal energy, it makes lithium surface diffusion on the lithium metal very unlikely at room temperature, thus leading to a dendritic surface growth tendency on lithium metal, as reported by Jäckle and Groß.[25] This causes safety issue as well as long-term cycling problem, which makes lithium metal very unfavorable to be used directly as the anode of lithium metal batteries.

However, lithium metal anode is one of the best anode material to be used in future batteries. So we need to solve this problem. Since we know that the dendrite growth of lithium metal is related to the high diffusion barrier (0.15 eV) of lithium on the surface, and the non-dendrite growth behavior of magnesium metal is explained by the low energy barrier (0.02 eV)[25], it is then highly possible in theory that we can alleviate or eliminate the dendrite growth problem of lithium metal by modifying its surface chemistry to reduce the energy barrier for lithium diffusion.

Surface alloying is well-known to change the property of the surface property of metals.[43] Therefore, the approach proposed in this work is to modify the surface diffusion property of lithium on the lithium metal by surface alloying lithium metal with another element. If an alloy protection layer can reduce the energy barrier of lithium diffusion on the surface, then it is highly possible that it can turn the dendritic lithium metal into a non-dendritic anode.

In the rest of this chapter, we report our DFT calculations on several lithium alloy systems. With lithium alloy formed directly on top of lithium metal, the lithium alloy will be in close contact with lithium source; therefore, the lithium alloy should be in the most

lithium-rich state. In this study, the most lithium-rich compound in the system were selected in all calculations. We studied As, Bi, Zn and In as the second element to form binary alloy with Li. According to their phase diagrams, the highest lithium-content stable phases (at room temperature) of these systems are Li_3As[44], Li_3Bi[45], LiZn[46] and $Li_{13}In_3$[47]. Our DFT calculations reveal that they have much lower energy barrier for lithium adatom diffusion on the surface (details in the following sections). Therefore, theoretically they should be good surface modifier of lithium metal anode to grow smooth and non-dendritic surface for lithium metal batteries.

3.2.2 Li-As system

Li_3As is the most lithium-rich compound in the Li-As system according to their phase diagram. It crystallized in a hexagonal close-packed (hcp) structure (space group: $P6_3/mmc$). The bulk properties of this material is simulated using its $1 \times 1 \times 1$ unit cell with structure data from ICSD. The calculated cell parameter a and c are collected in **Table 3**. They are in very good agreement with that of the experimental values[48]. The relaxed unit cell was used to construct slabs for DFT calculations to simulate the surface of Li_3As.

Table 3. Unit cell parameters of Li_3As from experiments[48] and our DFT calculations

Li_3As	**Exp. (Å)**	**Calc. (Å)**	**Δ** (%)
a/b	4.450[48]	4.374	1.707
c	7.880[48]	7.807	0.924

The surface energy of Li_3As was calculated similarly as that for lithium metal. Among the low index surfaces, the (110) surface has the lowest surface energy as calculated (**Table** 4). The other two surface have very high surface energy. This make sense since (110) surface is the most "close-packed" surface, while the other two surfaces are very open, and there are large gaps between the atoms on the surface of the alloy. A surface created by cutting through these surfaces will create much more dangling bonds, making the surface highly unstable compared to the relatively "close-packed" (110) surface. Therefore, the (110) surfaces of this alloy was selected in the following DFT calculations.

Table 4. Surface energies of different low index surfaces of Li_3As.

Miller Index	**(100)**	**(001)**	**(110)**
E_S (J/m^2)	1.111	1.272	0.501

The surface adsorption of lithium on the (110) surface of Li_3As was studied by a surface slab made of 2×2 geometry of (110) surface oriented along z axis (**Figure 8**). The slab has 5 atomic layers and a large vacuum layer. The top two layers of surface atoms were allowed to fully relax to simulate the surface relaxation of the (110) surface, while the middle layer atoms were fixed to simulate the bulk structure of Li_3As. The slab was fully relaxed before a lithium atom is positioned on the surface to simulate lithium adsorption.

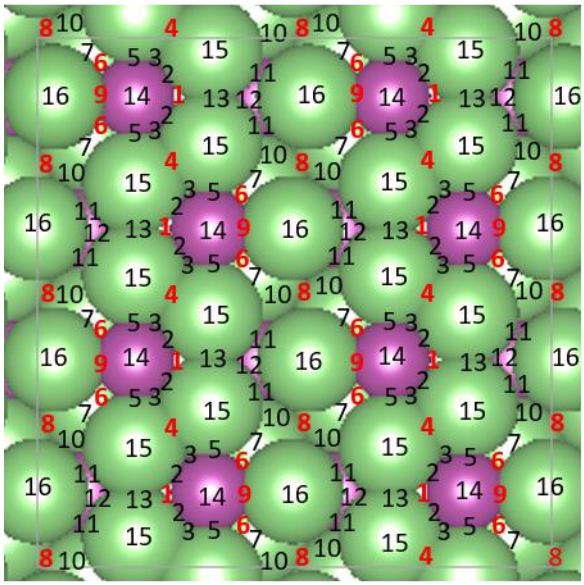

Figure 8. The Li_3As (110) slab 2 × 2 geometry of the (110) surface, along with its 16 high symmetry adsorption sites (numbered in black). The stable lithium adsorption sites, site 1, 4, 6, 8, and 9, are colored in red.

The PES of lithium adsorption on different positions of the surface was sampled representatively with 16 high symmetry sites. For each site on the slab, a lithium atom was positioned on the site. The lithium adatom were fully relaxed along with the top two layers of surface atoms on the slab. The lithium adatom positioned on site 1, 4, 6, 8 and 9 stayed at the same high symmetry site after relaxation. Therefore, these sites were identified as stable lithium adsorption sites, while the other sites are all energetically unstable sites. Li adatoms positioned on the other adsorption sites will lead to high-energy-state unstable configurations, where the adsorbed lithium atom will spontaneously diffuse to a nearby lower energy stable site with no or negligible diffusion barrier. Site 4 is the global minimum on the PES having the lowest energy. Other stable sites, 1, 6, 8, and 9, are local minima on the PES.

Similarly, the diffusion of lithium adsorbed on those stable sites were studied by CI-NEB technique. Li3As has MEPs with no barrier (from high energy sites 8 and 9, not drawn for clarity), or with very low barriers, 1→4: 0.008 eV, 1→6: 0.009 eV, 6→4: 0.004 eV (**Figure 9**).

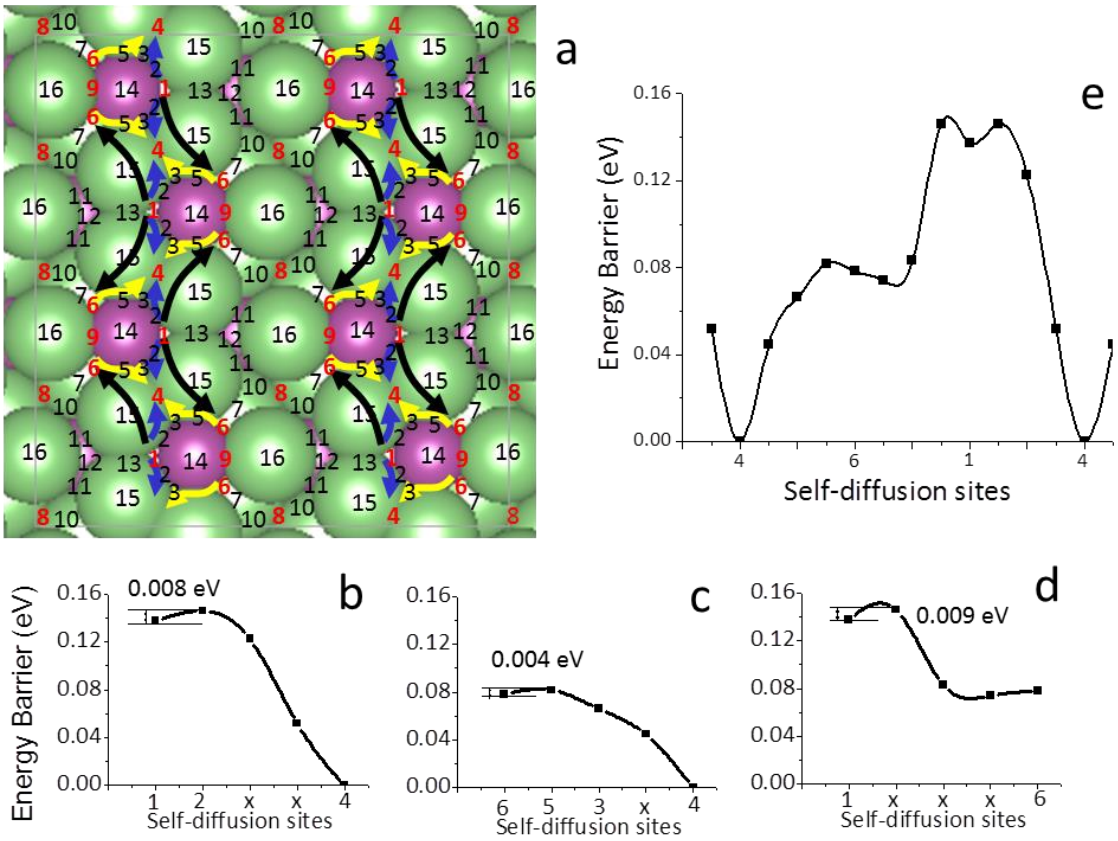

Figure 9. The calculated MEPs and their corresponding energy barriers of lithium diffusion among the stable adsorption sites (numbered in red) on Li_3As (110) surface. Energy barrier in between site 1 and site 4 (b), corresponding to blue arrow curves in (a); energy barrier in between site 6 and 4 (c), corresponding to yellow arrow curves in (a); energy barrier in between site 1 and 6 (d), corresponding to the black arrow curves in (a); the energetics of the long range diffusion path is shown in (e). The x labels on the x axis of the energy barrier diagram indicate the calculated MEPs are going through transition states which were not numbered in our calculations.

These energy barriers for the surface diffusion of lithium adatoms provided by Li_3As are even much lower than that of the well-known non-dendritic magnesium metal (0.02 eV)[25] and that of the thermal energy at room temperature (0.026 eV). They are negligible when compared to that of the dendritic lithium metal (0.150 eV).

In addition to those short range MEPs with extremely low energy barriers, there are also long range MEPs, $4 \rightarrow 6 \rightarrow 1 \rightarrow 4 \rightarrow \cdots$ (**Figure 9e**). These long range MEPs have roughly half the energy barrier for lithium diffusion compared to that of Li metal, with 0.082 eV for lithium diffusion from site 4 to site 6, and 0.072 eV for the diffusion from site 6 to site 1, leading to a maximum diffusion barrier of 0.082 eV.

Therefore, we predict that the lithium electrodeposited onto Li_3As-protected lithium metal during cell charging can easily diffuse across the surface at room temperature. And this makes Li_3As alloy a promising candidate for lithium metal anode protection layer for future lithium metal batteries.

3.2.3 Li-Bi system

In Li-Bi system, the compound with the highest lithium content is Li_3Bi, which crystallizes in face-centered cubic (fcc) lattice (space group: $Fm\bar{3}m$). The bulk properties of this compound is modeled with a $1 \times 1 \times 1$ unit cell with structure data from ICSD. The calculated cell parameter is reported in **Table 5** compared with the literature data[49]. This is in very good agreement with that of the experimental value, with only 0.3% in difference. The relaxed unit cell was used to construct slabs for DFT calculations to simulate the surface of Li_3As.

Table 5. Unit cell parameters of Li_3Bi from experiments[49] and our DFT calculations

Li_3Bi	**Exp. (Å)**	**Calc. (Å)**	**Δ** (%)
a/b/c	6.722[49]	6.744	0.329

Similarly, slabs were constructed for different surface of Li_3Bi, and the surface energy of each surface was calculated by DFT. The (110) surface of Li_3Bi has a lower surface energy compared to the other two low index surfaces (**Table 6**). This make sense since (110) surface has the highest density of atoms on its surface, with all atoms forming a hexagonal close packing if assuming an equal radius of Li and Bi atoms. The other two surfaces are very open, and there are large gaps between the atoms on the surface of the alloy. A surface created by cutting through these surfaces will create many more dangling bonds, making these surfaces highly unstable compared to the (110) surface. Therefore, the (110) surfaces of this alloy was selected in the following DFT calculations.

Table 6. Surface energies of different low index surfaces of Li_3Bi.

Miller Index	**(001)**	**(110)**	**(111)**
E_S (J/m^2)	0.759	0.550	0.693

Similarly to that of Li_3As, the surface adsorption of lithium on the (110) surface of Li_3Bi was studied by a surface slab made of 2×2 geometry of (110) surface oriented along z axis (**Figure 10**). The slab has 5 atomic layers and a large vacuum layer. The top two layers

of surface atoms were allowed to fully relax to simulate the surface relaxation on the (110) surface. The middle layer atoms were fixed to simulate the bulk structure of Li_3Bi. The slab was fully relaxed before a lithium atom is positioned on the surface to simulate lithium adsorption.

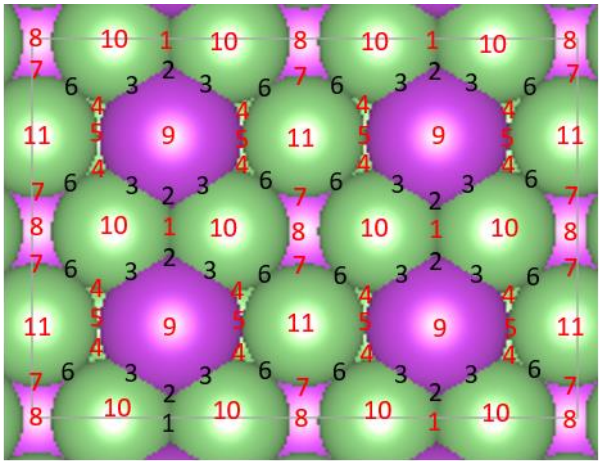

Figure 10. The Li_3Bi (110) slab with 2×2 geometry of the (110) surface, along with its 11 high symmetry adsorption sites (numbered in the figure). The stable lithium adsorption sites, site 1, 4, 5, 7, 8, 9, 10 and 11 are colored in red.

The PES of lithium adsorption on different positions of the (110) surface of Li_3Bi was sampled with 11 high symmetry sites. To simulate the lithium adsorption on different sites, a lithium atom was positioned on each site. The lithium adatom were fully relaxed along with the top two layers of surface atoms in the slab. The lithium adatom positioned on site 1, 4, 5, 7, 8, 9, 10 and 11 (colored in red in **Figure 10**) stayed at around the same high symmetry sites after relaxation. Therefore, these sites are stable lithium adsorption sites, while the other sites are all energetically unstable sites. Li adatoms positioned on the other adsorption sites will lead to highly unstable configurations, where the adsorbed lithium atom will spontaneously diffuse to a nearby lower energy stable site with no or negligible diffusion

barrier. Site 1 has the lowest energy. Therefore, it is the global minimum on the PES. Other stable sites, 4, 5, 7, 8, 9, 10 and 11, are local minima on the PES.

All the possible diffusion paths of a lithium adatom between one stable site and a neighboring stable site were studied by CI-NEB calculations. The results are collected in **Figure 11**.

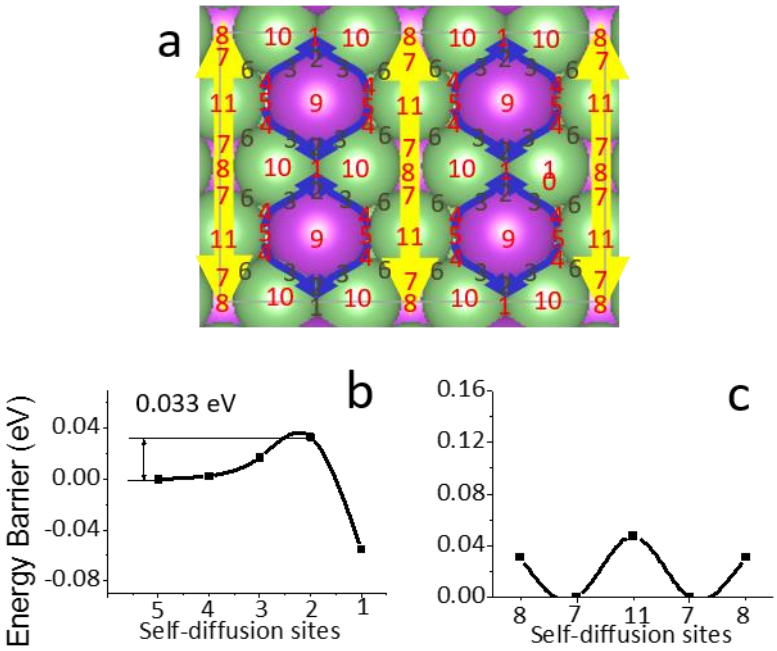

Figure 11. The calculated minimum energy paths (a) and their corresponding energy barriers of lithium diffusion (b,c) among stable adsorption sites (numbered in red) on Li_3Bi (110) surface. (b) diffusion barrier of short range MEPs along site 5, site 4 towards site 1, corresponding to the blue arrow lines in (a); (c) diffusion barrier of long range MEPs with a diffusion barrier of 0.055 eV through site 7, 8 and 11, corresponding to the yellow arrow lines in (a).

According to our calculations, Li3Bi has short range MEPs with no barrier (from high energy sites 8, 9, 10 and 11, some paths not drawn for clarity), MEPs with low barriers (5→ 4 →1: 0.033 eV, 7→8: 0.039 eV, 7→11: 0.055 eV) as well as long range MEPs, along the

path 7 ↔ 8 ↔ 7 ↔ 8 ↔ 11 ↔ 7 ↔ 8 ↔ ⋯ (yellow arrow lines in **Figure 11**), having a maximum energy barrier of 0.055 eV.

These energy barriers provided by Li_3Bi stable surface are comparable to that of the well-known non-dendritic magnesium metal (0.02 eV)[25] and the thermal energy at room temperature (0.026 eV). They are significantly lower than that of the dendritic lithium metal (0.150 eV). Therefore, we predict that Li_3Bi can provide diffusion paths with much lower diffusion barriers compared to that of lithium metal. This compound will provide significantly improved diffusibility for electrodeposited lithium on the surface during cell charging. This renders Li_3Bi alloy another promising candidate to stabilize lithium metal anode.

3.2.4 Li-Zn System

The most lithium rich compound in the Li-Zn system is LiZn, which crystallizes in fcc structure with 8 formula units per unit cell (space group $Fd\bar{3}m$). The bulk properties of LiZn was first modelled with a single unit cell starting from the crystal structure data from ICSD. After DFT calculations on its structure optimization and relaxation, the calculated unit cell parameter was in very good agreement with the experimental data[50], with only 1% in difference (**Table 7**). The relaxed unit cell was used to construct slabs for DFT calculations to simulate the surface of LiZn.

The most stable LiZn (110) surface was modeled with a slab made of 2×2 geometry of (110) surface oriented along z axis (**Figure 12**). It has 5 atomic layers and a large vacuum layer. The top two layers of surface atoms were allowed to fully relax to simulate the surface

relaxation on the (110) surface. The middle layer atoms were fixed to simulate the bulk structure and property of LiZn. The slab was fully relaxed before a lithium atom is positioned on the surface to simulate lithium adsorption.

Table 7. Unit cell parameters of LiZn from experiments[50] and our DFT calculations

LiZn	**Exp. (Å)**	**Calc. (Å)**	**Δ** (%)
a/b/c	6.235[50]	6.161	1.186

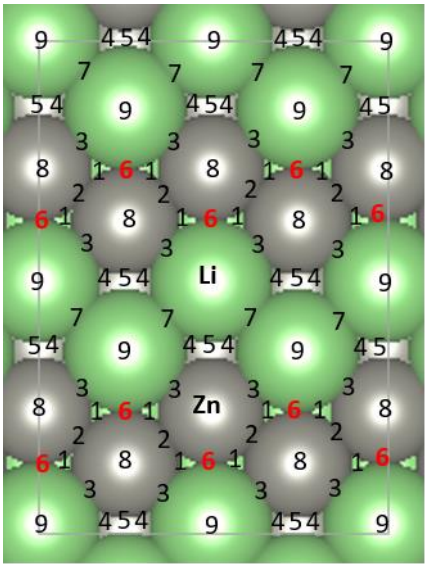

Figure 12. The 9 high symmetry adsorption sites selected to map LiZn (110) surface, with the stable lithium adsorption sites (site 6) colored in red. Color code: Green spheres are lithium, grey spheres are zinc.

The PES of lithium adsorption on the (110) surface of LiZn were sampled by placing a lithium adatom on each of the 9 high symmetry sites (as numbered in **Figure 12**). The stable lithium adsorption sites of this surface was determined after fully relaxing the slab surface along with the adsorbed lithium atom. If a lithium adatom does not move away from the

initial high symmetry adsorption site, this site is then found to be a stable adsorption site (numbered in red color in **Figure 12**). After surface relaxation, the lithium adatom positioned at all sites ended up in site 6. This means site 6 is the only stable adsorption site and the global minimum site on the PES of LiZn (110). All the other sites are high energy unstable adsorption sites, any lithium adatom will diffuse easily to a global minimum site 6. If LiZn protected lithium metal is employed as the anode of a LIB, a lithium ion, during cell charging, will be reduced and adsorb onto the site 6 when it receives an electron in the vicinity of this stable site. On the other hand, if the lithium ion gets reduced from any other high symmetry adsorption sites, the lithium adatom will adsorb on site, but then spontaneously diffuse towards the stable site 6 with no or negligibly low energy barrier.

Then CI-NEB was then adopted to study the surface diffusion of lithium on this surface from one stable adsorption site towards the next one. The result is presented in **Figure 13**. The LiZn alloy offers a very low barrier of 0.023 eV (**Figure 13c**) for the lithium adatom to diffuse along a long range MEPs from the global minimum site 6 to the next one through a transition state site 2 (**Figure 13a,b**). This energy barrier is comparable to that of the well-known non-dendritic magnesium metal (0.02 eV).[25] They are both lower than the thermal energy at room temperature (0.026 eV), and they are more than five times lower than that of the dendritic lithium metal (0.150 eV). Therefore, we predict that any lithium electrodeposited onto the LiZn stable surface (110) during cell charging can easily diffuse around the surface at room temperature. And this makes LiZn alloy a promising candidate for lithium metal anode protection layer for future lithium metal batteries.

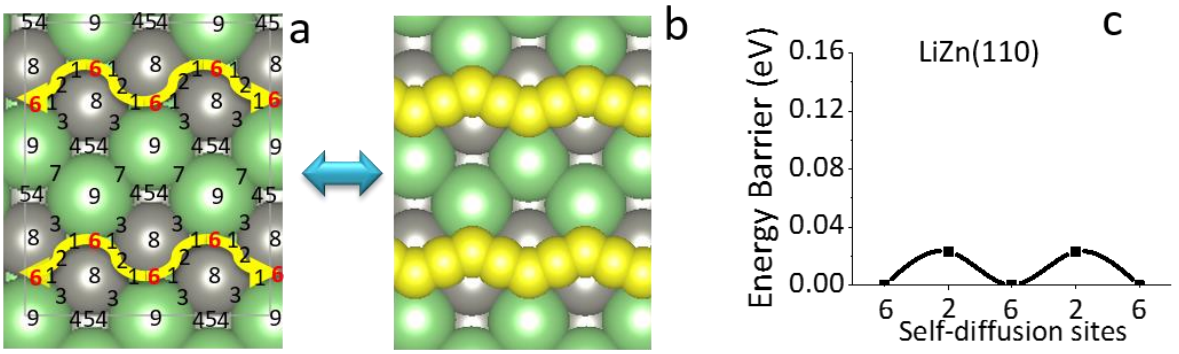

Figure 13. Long range MEPs of lithium adatom diffusion on the (110) surface of LiZn and the activation energy of the diffusion process calculated by CI-NEB. The yellow lines in (a) and (b) correspond to the long range MEPs of lithium adatom with an (c) energy barrier of 0.023 eV. The red numbers are stable adsorption sites (minima on the potential energy surface (PES)), all other numbered sites are unstable and spontaneously relax to one of those stable sites. Color code: yellow spheres (lithium adatoms), green spheres (Li surface atoms), grey spheres (Zn surface atoms).

3.2.5 Li-In system

The compound with the highest lithium content in Li-In system is $Li_{13}In_3$. It also crystallizes in a fcc structure (space group: $Fd\bar{3}m$). The bulk properties of $Li_{13}In_3$ was first modelled with a single unit cell starting from the crystal structure data from ICSD. After DFT calculations on its structure optimization and relaxation, the calculated unit cell parameter (**Table 7**) was in very good agreement with the experimental data[51]. The relaxed unit cell was used to construct slabs for DFT calculations to simulate the surface of $Li_{13}In_3$.

Table 8. Unit cell parameters of $Li_{13}In_3$ from experiments[51] and our DFT calculations

$Li_{13}In_3$	**Exp. (Å)**	**Calc. (Å)**	**Δ** (%)
a/b/c	13.556[51]	13.327	1.691

The most stable $Li_{13}In_3$ (110) surface was modeled with a slab made of 1×1 geometry of its (110) surface oriented along z axis (**Figure 14**). The slab is composed of 6 atomic layers and a large vacuum layer to ensure a consistent stoichiometry of the slab compared to that of the bulk material of $Li_{13}In_3$. The top two layers of surface atoms were allowed to fully relax to simulate the surface relaxation on the (110) surface.

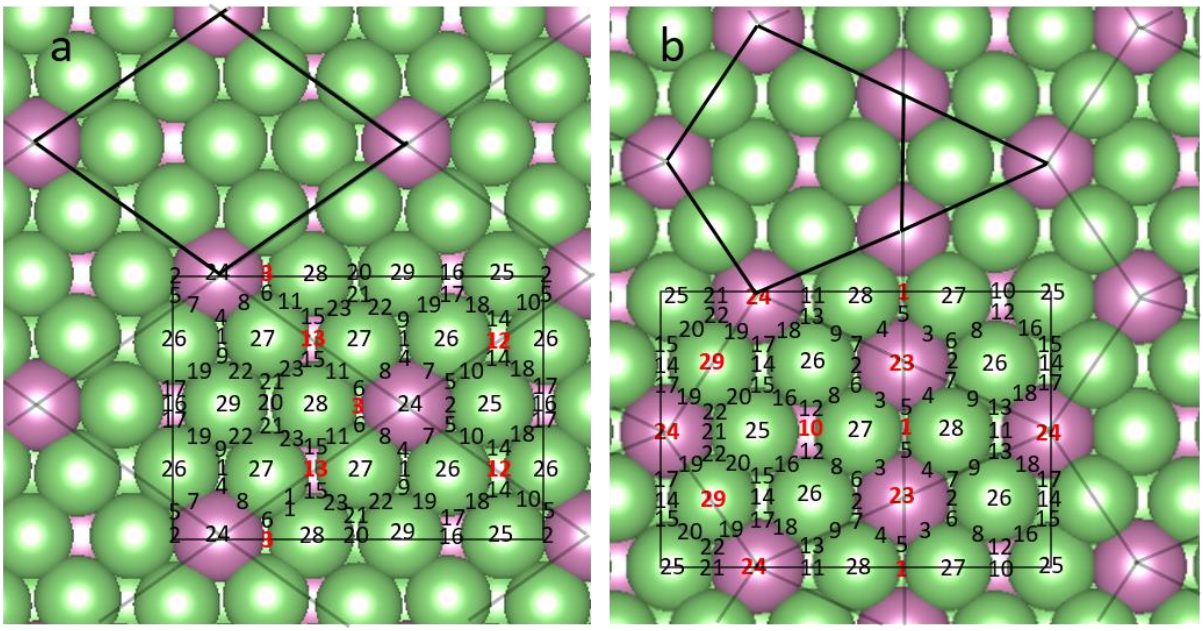

Figure 14. Illustration of (110) surface of $Li_{13}In_3$ with two terminations: (a) termination with a pattern formed by rhombuses, named T4; (b) termination with a pattern formed by pentagons and triangles, denoted as T53. The PES of lithium adsorption on these two surface were sampled by 29 high symmetry sites in both T4 and T53 surfaces (numbered), with stable adsorption site numbers colored in red. Color code: lithium (green), indium (violet).

The two middle layer atoms were fixed to simulate the bulk structure and property of $Li_{13}In_3$. The slab was fully relaxed before a lithium atom is positioned on the surface to simulate lithium adsorption. This slab has two different surface terminations, one on the top surface, one on the bottom surface: one termination has indium atoms arranged in a pattern of

rhombuses (denoted as T4, **Figure 14a**) and the other one has indium atoms forming pentagons and triangles (denoted as T53, **Figure 14b**).

The PESs of lithium adsorption on the T4 and T53 surfaces of $Li_{13}In_3$ were both sampled by placing a lithium adatom on each of the 29 high symmetry sites, respectively (as numbered in **Figure 14a,b**). After fully relaxing these slab surfaces along with their adsorbed lithium atom, the lithium adatoms positioned on the red numbered sites in **Figure 14** did not move away from their initial high symmetry adsorption sites. These sites are then determined to be a stable adsorption sites. The stable sites on the T4 surface are site 3, 12 and 13, while the stable adsorption sites on the T53 surface are site 1, 10, 23, 24 and 29. All the other sites are high energy unstable adsorption sites, and the lithium reduced and electrodeposited on these sites will diffuse spontaneously to a lower energy stable adsorption site in the vicinity with no energy barrier or a negligibly small one.

Lastly, the CI-NEB method was adopted to study the surface diffusion of lithium from one stable adsorption site towards the next one on T4 and T53 terminations of the $Li_{13}In_3$ (110) surface. On T4 surface, site 3 has the lowest energy, so it is the global minimum on the PES. The other stable lithium adsorption sites, site 12 and 13, are approximately energy degenerate local minima on PES, and they have no or negligibly low energy barrier to diffuse towards the global minimum site 3 according to our CI-NEB calculations. The diffusion paths are as shown along the blue lines in **Figure 15**. Take into consideration of the thermal energy at room temperature (0.026 eV), it's known that lithium adsorbed on this surface can diffuse freely on the surface.

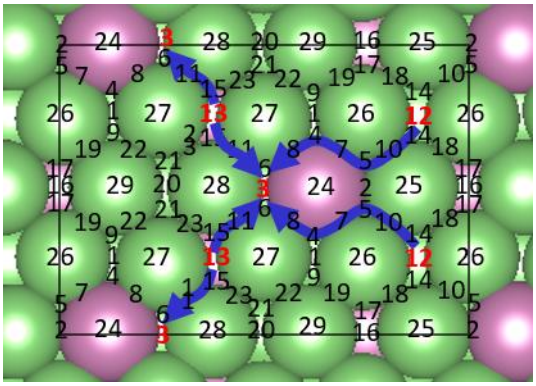

Figure 15. MEPs of lithium adatom diffusion on the T4 termination of $Li_{13}In_3$ (110) surface calculated by CI-NEB. The blue arrow lines are calculated diffusion paths from site 13 and 12 with no apparent diffusion barriers. Color code: lithium (green), indium (violet).

On T53 surface, site 23 and 24 are approximately energy degenerate sites with the lowest energy, they are the global minima on the PES. Site 1 has a slightly higher energy state than that of the global minima (**Figure 16c**). The other stable sites, site 10, and 29, are higher energy local minima on PES, and they can diffuse towards other lower energy stable sites with either no barrier (blue lines in **Figure 16a**). There are also local MEPs with fairly low energy barriers: 0.013 eV for lithium diffusion from site 10 to 24 (**Figure 16b** and brown lines in **Figure 16a**), 0.028 eV for diffusion from site 10 to site 1 (**Figure 16b** and black line in **Figure 16a**). Additionally, T53 surface also provides a long range diffusion path with an energy barrier of 0.029 eV cross site 1 and site 23 (yellow arrow line in **Figure 16a**). The diffusion barriers on this surface are also low enough for lithium diffusion across the surface at room temperature, even the highest diffusion barrier along the long range diffusion path is 4 time smaller than that of the dendritic lithium metal (0.150 eV). And most energy barriers of the calculated MEPs are either lower than or comparable to that of the well-known non-

dendritic magnesium metal (0.02 eV)[25] and the thermal energy at room temperature (0.026 eV).

Overall, $Li_{13}In_3$ will provide significant improvement in the surface diffusibility for electrodeposited lithium during cell charging. Therefore, we predict that $Li_{13}In_3$ could be an effective protection layer candidate for lithium metal anode.

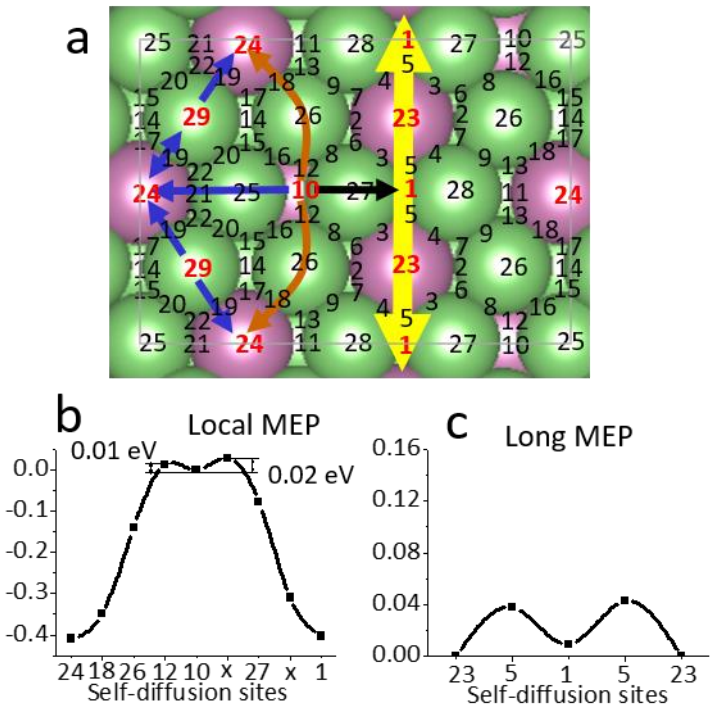

Figure 16. MEPs of lithium adatom diffusion on the T53 termination of $Li_{13}In_3$ (110) surface and the activation energy of different diffusion paths calculated by CI-NEB. (a) MEPs across between stable lithium adsorption sites, with diffusion barriers of (b) short range MEPs from site 10, left branch corresponds to the brown lines and right branch corresponds to the black arrow line in (a); (c) long range MEP along site 1 and site 23, corresponding to the yellow arrow line in (a). Color code: lithium (green), indium (violet).

3.3 Conclusion

Our DFT calculations indicate that these lithium-rich alloys provide much lower energy barrier for surface diffusion of lithium, which theoretically lead to a novel approach to tackle the dendrite formation problem of lithium anode by surface alloying. Due to the much lower energy barriers on those surface alloys, lithium adatom can easily diffuse around the surface thus leading to an epitaxial growth behaviour. A smooth lithium electrodeposition morphology is predicted for lithium metal protected by these alloys, instead of growing dendrites on the surface. The prediction was validated by the experimental data in the following chapter.

What's more, this work focused only on 4 lithium compounds, but there are other elements which can form compounds with lithium. More work can be done on those materials to study the lithium diffusion on their surfaces. And there are other ways to modify the surface of lithium metal to reduce the diffusion barrier of lithium on their surfaces. There could be much more exciting discoveries by taking advantages of this surface modification approach to stabilize the lithium metal anode for future lithium metal batteries.

Chapter 4

A Stable Lithium Anode Using Lithium Surface Alloying

4.1 Experimental

All promising lithium alloys calculated in previous chapter were employed to protect lithium metal anode experimentally. The synthesis, characterization along with electrochemical testing of those alloy-protected lithium metal anode were reported in this chapter.

4.1.1 Preparation of the protected lithium electrode

Electrode preparation was carried out in an argon-filled glove box with <1 ppm oxygen and moisture. Lithium metal foil (99.9%, Aldrich) was polished until the surface was extremely shiny. After polishing, the lithium foil was immersed in 0.167M MCl_x solution in THF for 20 seconds (M= As, In, Zn or Bi). Upon removal from the THF solution, the excess liquid on the treated lithium foil was carefully cleaned using a Kimwipe. The foil was then rinsed with THF and further dried in vacuum for 2 days at room temperature. It was finally cut into circles with 11 mm in diameter for further investigation.

4.1.2 Electrochemical measurements

The electrochemical studies were carried in 2032 coin cells. For the impedance and lithium plating/stripping studies, symmetric cells (fresh lithium on each side or protected lithium foil on each side) were assembled with 40 µL of 1M LiTFSI in DOL/DME (1:1 vol) as the

electrolyte. The protocol used was 1 hour of stripping followed by 1 hour of plating with a current density of 2 mA/cm^2. To investigate the performance of the protection compared to the lithium metal anode, cells were made with $Li_4Ti_5O_{12}$ (LTO) as the cathode. The LTO electrodes were prepared by casting a DMF slurry containing $Li_4Ti_5O_{12}$ (Sigma-Aldrich), Super P and PVDF in a weight ratio of 8:1:1 onto the carbon coated Al foil. The cathodes were cut to disks with a diameter of 11 mm and dried at 60 ^oC prior to use. The areal loading of LTO was about 3 mg/cm^2. Approximately 40 µL of 1M LiTFSI in DOL/DME (1:1 vol) was used as the electrolyte for the LTO cells. Electrochemical impedance measurements were conducted at room temperature using a VMP-3 and a frequency range of 0.1 Hz to 100 kHz. The cycling of the half-cell was conducted on an Arbin cycler, in a voltage window between 1 – 2.5 V.

4.2 Results and Discussion

The understanding of the diffusion properties of the Li based alloys *vs.* pristine lithium metal opens up an opportunity to tune the lithium electrodeposition behavior by surface modification. We designed a facile procedure to fabricate these aforementioned thin alloy layers coated onto lithium metal foil by *in-situ* reduction of metal chlorides (**Equation 24,** M = In, Zn, Bi, As) by Li:

$$x\mathrm{Li} + \mathrm{MCl}_x \rightarrow \mathrm{M} + x\mathrm{LiCl} \qquad 24$$

The metal layer instantly undergoes reaction at room temperature with the underlying lithium metal that proceeds until a single phase composition at equilibrium is achieved (**Equation** 25).

$$y\mathrm{Li} + z\mathrm{M} \rightarrow \mathrm{Li}_y\mathrm{M}_z \quad (25)$$

Accordingly, the color of the protected lithium metals changes, *e.g.* LiZn protected lithium turns from matte silver to yellow-green. The kinetics of **Equation 24** are very fast, as the color of the shiny lithium metal changes within seconds upon dipping in solution (**Figure 17a**). The composition of the equilibrated protection layer was characterized by X-ray diffraction (**Figure 17b**), showing that $Li_{13}In_3$, LiZn, Li_3Bi, and Li_3As are the only crystalline phases on the respective protected lithium foils. These phases correspond to the stable states with highest lithium concentration at room temperature. This is because the thin alloy layer is in close contact with the excess lithium underneath. **Figure 17c** shows an SEM image of the smooth surface of fresh lithium. After reaction with the metal chlorides and aging for 2 days in vacuum, the lithium foil was uniformly covered by the corresponding alloys (**Figure 17e, g**). EDS mapping of the indium protected lithium clearly shows a uniform distribution of indium in the layer (**Figure 17d**). The alloy layer is typically less than 10 μm thick (**Figure 17f, h**) as measured by cross-sectional SEM. They function completely differently than their corresponding bulk alloys (Li-Mg, Li-Na, Li-Al, Li-In) employed as the anode, which serves as the lithium source with deleterious volume expansion.[52,53] In our approach, the primary lithium source is the underlying foil. The ultra-thin, Li_xM protective layers predominantly function as electron/ion conductors during lithium plating/stripping and stabilize the underlying lithium foil free of dendrite growth, as will be discussed next. Assuming a 200 μm lithium foil (although larger thickness can be employed), overall the protecting alloy layer is thus only < 5 % in thickness. In addition, because the "alloys" are line phases at room

temperature - not solid solutions - they are compositionally invariant during cycling, and exist as the lithium rich phase by virtue of contact with the lithium foil.

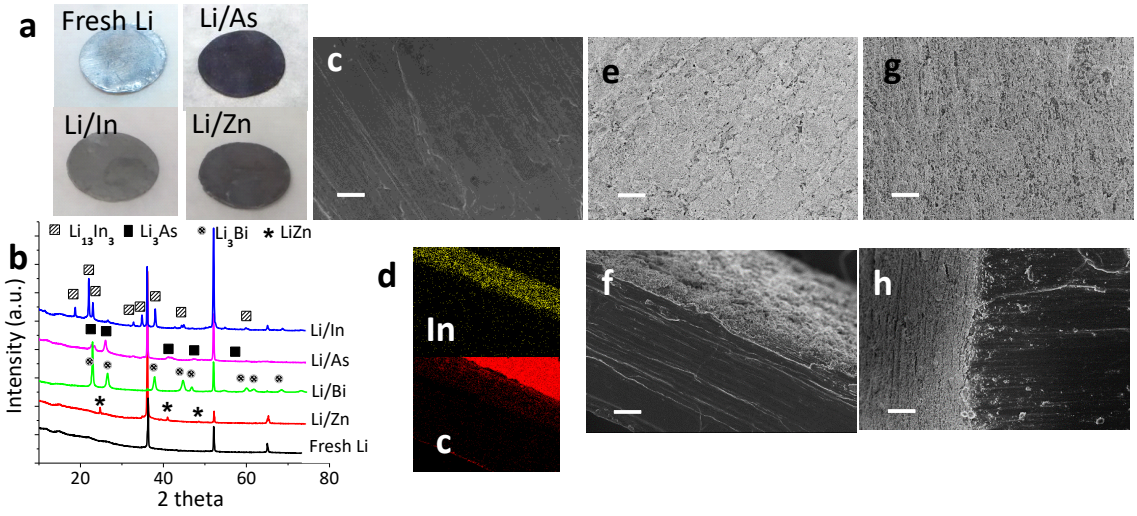

Figure 17. Characterization of the alloy protected lithium. (a) Photos of fresh lithium metal vs. the alloy protected lithium samples. (b) X-ray diffraction patterns of fresh lithium metal and the alloy-protected lithium metal. (c) SEM image of fresh lithium, (d) EDS mapping of the cross-section indium protected lithium. SEM image of (e) indium alloy protected lithium, (g) zinc alloy protected lithium. Characterization of the protected lithium from the cross-sectional view: (f) indium alloy protected lithium, and (h) zinc alloy protected lithium. The scale bar is 20 μm.

The composition of the protected lithium was further demonstrated by X-ray photoelectron spectroscopy (XPS) analysis. Indium protected lithium is used for illustration (**Figure 18a**). Bulk Li-In alloy prepared by cold press is provided for reference. The major peak at 442.2 eV (**Figure 18ai**, red) is assigned as the In in alloy (redueced form of $In^{\delta-}$),[54] whereas two other smaller components with higher binding energy are donated by the indium metal (443.2 eV) and oxide (444.5 eV),[55] respectively. On the surface of alloy protected lithium (**Figure 18aii**), the Li-In alloy is clearly present, along with a significant amount of

indium metal andoxide. Nevertheless, the fraction of indium metal in the protection layer dramatically decreased after Ar-sputtering for 5 minutes (**Figure 18aiii**), and further decreased after sputtering for 10 minutes (**Figure 18aiv**), indicating an decreasing fraction of alloyed In under the surface.

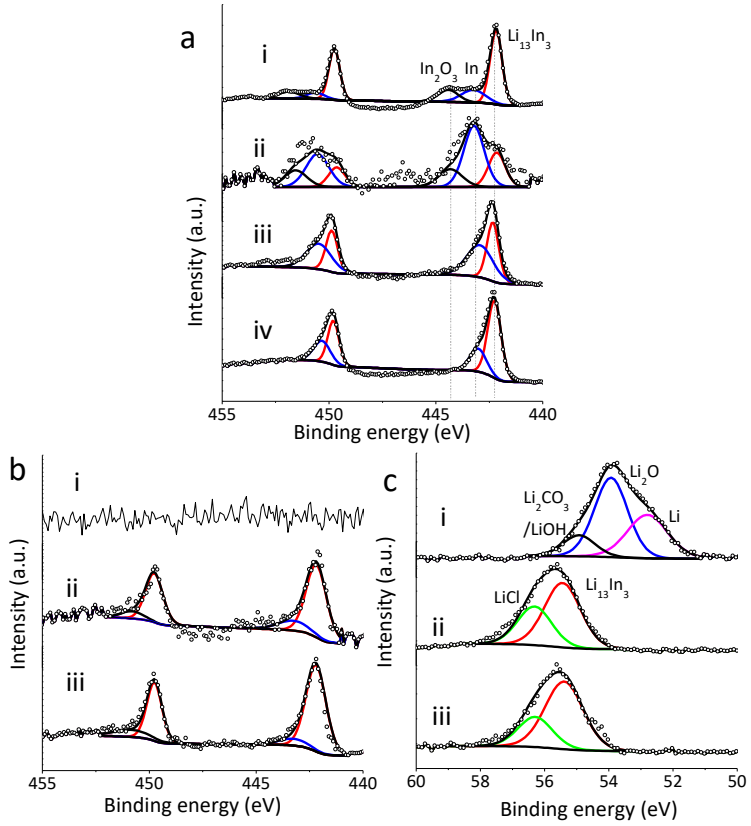

Figure 18. XPS analysis of the indium alloy protected lithium metal. (a) In 3d core level spectra of (i) the Li-In alloy made by cold press as the reference, the Li-In alloy protected lithium: (ii) pristine sample, (iii) after 5 min Ar sputter, (iv) after 10 min Ar sputter. (b) and (c) are In 3d and Li 1s spectrum after plating with 2 mAh cm^{-2} of lithium, respectively, (i) pristine sample, (ii) after plating, after 5 min Ar sputter, (iii) after 10 min Ar sputter.

This observation indicates that the self-alloying process is dominated by the kinetics of reaction in **Equation** 25 and results in a gradient of alloy concentration at different deepness.

The free indium will alloy with the plated lithium when the protected lithium metal is operated in a cell, this phenomenon will be discussed in next section.

4.2.1 Understanding the electrodeposition of the alloy protected lithium

We employed a combination of SEM, optical microscope, and XPS with depth profiling to understand the electrodeposition of the Li-rich alloy protected lithium metal. Indium alloy and zinc alloy protected lithium metals were used as the representative in this section. **Figure 19a-c** report the SEM images of the lithium electrodes after the Li plating/stripping at the current density of 2 mA cm^{-2}.

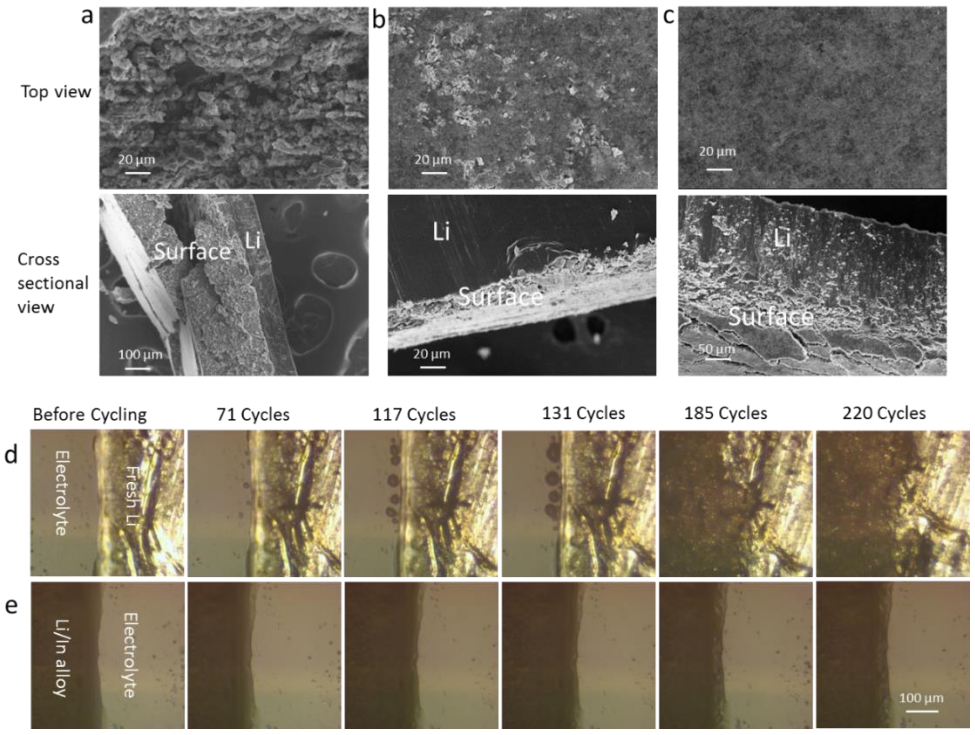

Figure 19. Microscopy study of the alloy protected lithium metal. SEM images of the lithium anode after 100 cycles of plating/stripping, (a) fresh lithium, (b) indium protected lithium anode, (c) zinc protected lithium anode. Photos of the electrodes from the transparent cell during plating/stripping, (d) fresh lithium, (e) indium protected lithium anode.

Electrodes were gently washed with THF to remove the electrolyte salt and dried under vacuum prior to the SEM characterization. The electrode surface was pulverized after 100 cycles (200 hours) of repeated Li plating/stripping for the pristine lithium electrode (**Figure 19a** *vs.* **Figure 17c**). This is attributed to continuous Li consumption by the repeated formation/consumption of the SEI layer, which is exacerbated by formation of high surface area dendrites. On the contrary, the alloy protected lithium anodes shows no visible change on the surface after plating/stripping, evidencing smooth, non-dendritic lithium deposition, (**Figure 19b,c** *vs.* **Figure 17e,g**). The cross-sectional view further demonstrates that the corrosion of the surface is effectively hindered even after long cycling.

To illustrate the suppression of dendrites growth by the alloy surface layers, we monitored the plating/stripping process using a transparent cell with a configuration shown in **Figure 20a**. Two electrodes – one lithium metal and the other indium protected lithium – were separated by a thin film of polyvinyldenedifluoride (PVdF) membrane soaked with liquid electrolyte (1M LiTFSI in 1:1 DOL/DME). The cell was sealed by two microscope slides. Alternate plating/stripping (4 mA cm^{-2}, 10 min) was applied to the electrodes and the cell was monitored by an optical microscope equipped with a digital camera (**Figure 20b**). **Figure 19d,e** show the photos taken at different cycles of plating/stripping. Before cycling, the surfaces of both lithium and indium-protected lithium were clean and smooth. Protrusions (incipient dendrites) appear along the edge of the lithium electrode during the plating/stripping experiment, evidence of inhomogeneous lithium deposition (**Figure 19d**). This is due to poor Li atom mobility on the lithium surface owing to the high diffusion

energy barrier (**Figure 7**). These protrusions nucleate, and aggregate to form high surface area dendrites, eventually pulverizing the lithium surface (after 185 cycles), which is consistent with the porous morphology of the lithium electrode after repeated plating/stripping (**Figure 20a**). In contrast, alloy-protected lithium metal with a lower surface diffusion activation barriers exhibit smooth lithium deposition. The surface shows no sign of dendrites or pulverization on the surface on cycling (**Figure 20e**).

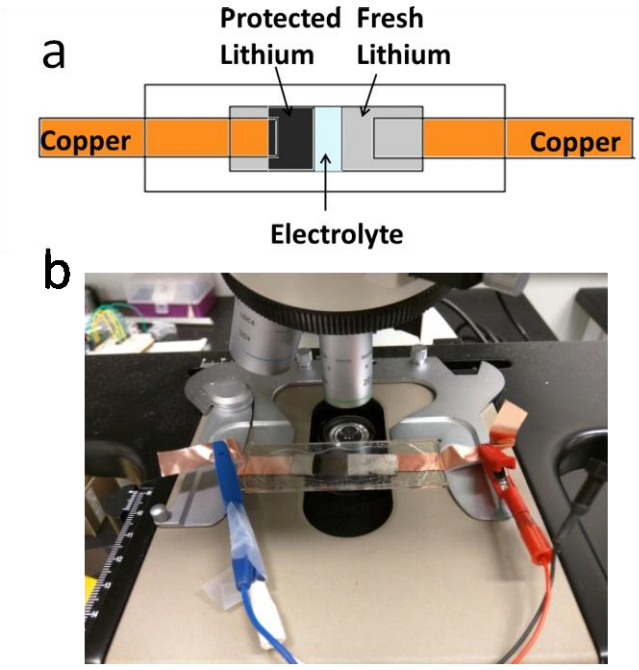

Figure 20. (a) Schematic showing the configuration of the optically transparent cell, (b) cell was plating/stripping with a current density of 4 mA cm^{-2} for 10 minutes on the microscope.

Figure 18b, c report the XPS depth profiling of the indium alloy protected electrode after plated with 2 mAh cm^{-2} of lithium. Before sputtering, the absence of In signal (**Figure 18b$_i$**) and presence of lithium components (**Figure 18c$_i$**) implies that the protection layer was covered by electrodeposited Li (52.8 eV) together with the SEI consisted of LiOH/Li_2CO_3

(55.0 eV) and Li_2O (53.7 eV).[56] This SEI composition is very similar to that of the pristine lithium metal, which is naturally cover by the $LiOH/Li_2CO_3$ and Li_2O passivation layer (**Figure 21a,b**). EDS analysis confirms that the indium atom concentration on the electrode surface is slightly decreased from 19% to 14% after plated with 2 mAh cm^{-2} of lithium at a current of 50 μA cm^{-2} (**Figure 22**), indicating the electrode surface was only covered by very thin layer of the plated Li/ SEI.

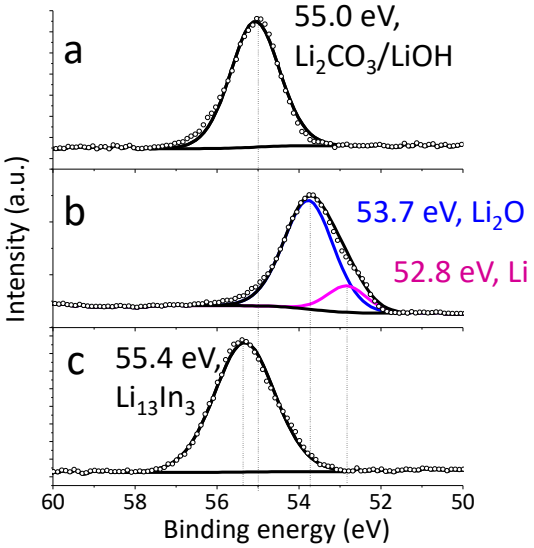

Figure 21. Li 1s core level spectra. (a) pristine lithium metal, (b) lithium metal after 45 minutes of Ar sputtering. (c) $Li_{13}In_3$ made by cold press. The pristine lithium metal was covered by a passivation layer of Li_2CO_3/LiOH and Li_2O.

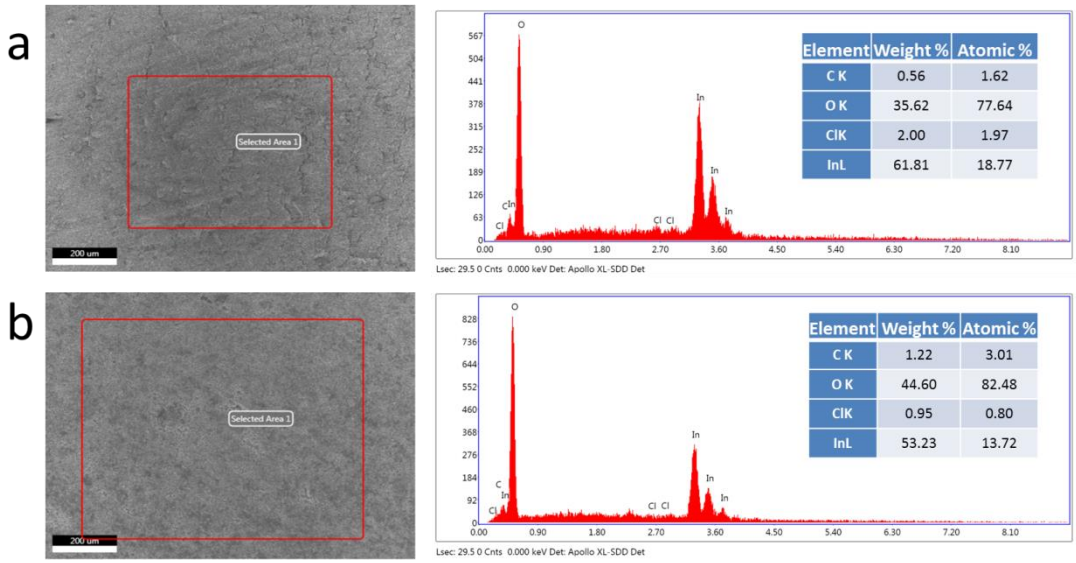

Figure 22. EDS analysis of the indium alloy protected lithium before the lithium plating (a), and (b) after plated with 2 mAh cm^{-2} of lithium by current of 50 μA cm^{-2} for 40 hours.

Ar ion sputtering is employed to determine the composition of the near surface. After 5 minutes' sputtering, which roughly removes 10 nm in thickness considering the sputtering rate of 1-2 nm/min,[56] the In 3d spectrum shows the predominance of $Li_{13}In_3$ with a minor contribution from indium metal (**Figure 18b$_{ii}$**), whereas no metallic lithium or SEI composition is present in the Li 1s spectrum (**Figure 18cii**).. This indicates that the thickness of the aforementioned lithium/SEI layer is actually only about 10 nm, far less than 10 μm, the approximate thickness of deposited lithium (2 mAh cm^{-2}). This observation suggests that majority of the plated lithium atoms have gone into or through the protection layer. The corresponding Li 1s spectrum (**Figure 18c$_{ii}$, Figure 22c**) clearly shows the $Li_{13}In_3$ phase (55.4 eV) and some LiCl (56.2 eV, introduced from the synthesis process).

We note that the metallic indium is far reduced after plating (**Figure 18bii** and **Figure 18biii**) comparing to the pristine Li-In protected lithium (**Figure 18a$_i$**). This suggests that the

plated lithium first alloys with the residual indium metal on the surface layers until it reaches equilibrium at the lithium-rich phase, $Li_{13}In_3$.

4.2.2 Electrochemical testing of the alloy protected lithium anode

To evaluate our hypothesis that the alloy protected lithium metal exhibits higher resistance to dendrite formation and is thus more resistant to failure by dendrite-induced short-circuits, stripping/plating measurements were carried out in symmetric Li-Li cells. In these experiments, practical surface capacity of lithium at high current density (2 mAh cm^{-2} at 2 mA cm^{-2}) was repeatedly deposited/dissolved in each discharge and charge cycle. **Figure 23a-c** shows the voltage profiles as a function of time. The lithium metal without the alloy protection short circuits within 200 h (100 cycles). The fluctuating voltage profile (**Figure 23a**) is the sign of cell failure induced by dendrite formation. In contrast, the alloy protected lithium shows a very stable voltage profile under the same test conditions (**Figure 23b, c**). Both the indium and zinc protected lithium cells cycle for more than 1000 hours without any sign of a short circuit. Arsenic and bismuth alloy protected lithium metal anodes show similar performance: they can be repeatedly plated/stripped for over 1200 and 1400 hours, respectively (**Figure 24**). The over five-fold improvement in cycling life proves that the protection layer is effective in stabilizing lithium electrodeposition. These alloy-protected lithium anodes also exhibit stable performance when the plating/stripping experiments were conducted in a classic Li-ion electrolyte (1M $LiPF_6$ in EC-DMC, **Figure 25**), demonstrating that the improvement is not restricted by the type of electrolyte. To the best of our knowledge, this is the best performance of Li plating/stripping in symmetric cells at such a

high current density/ surface capacity compared to any other work trying to stabilize the lithium metal anode by electrolyte additives[9,15], artificial SEIs[11,12] or solid electrolytes[18,57].

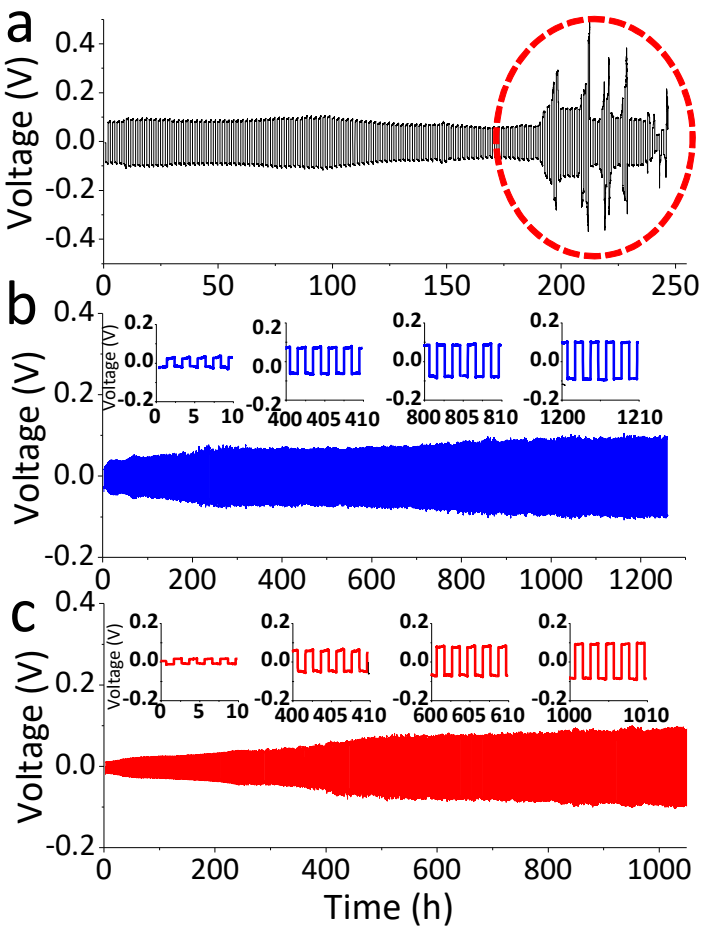

Figure 23. Electrochemical performance of the protected lithium metal. Lithium stripping/plating in symmetric cells at a current density of 2 mA cm^{-2} for 1 hour in 1M LiTFSI 1:1 DOL:DME electrolyte. Voltage profile of (a) fresh lithium metal anode, (b) indium protected lithium anode, (c) zinc protected lithium anode.

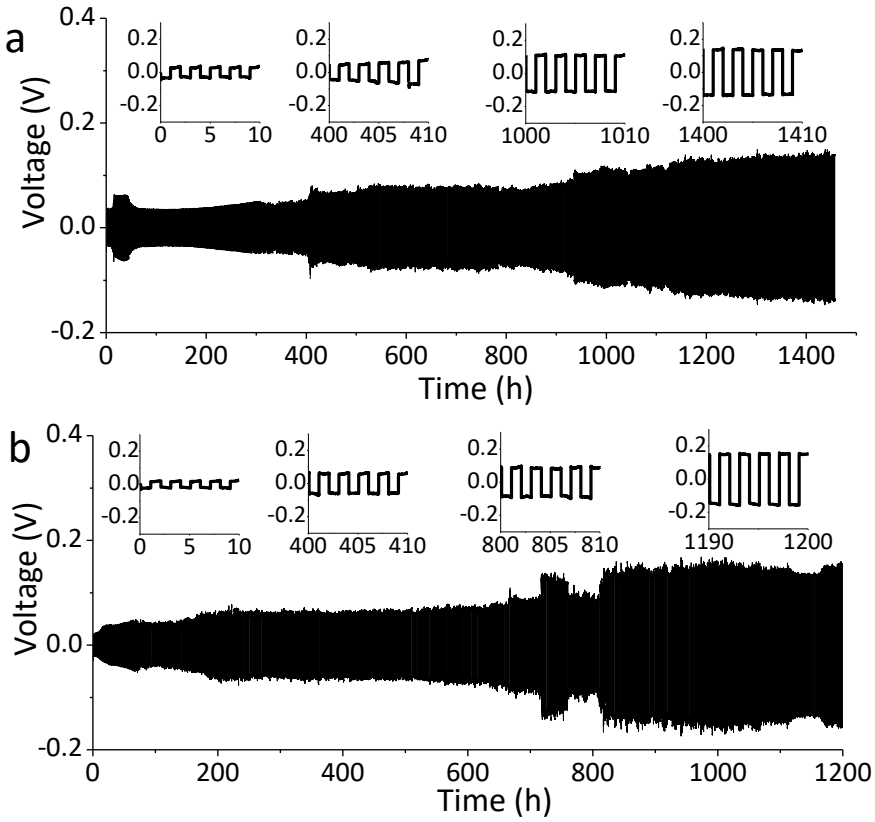

Figure 24. Lithium stripping/plating in symmetric cells at a current density of 2 mA cm^{-2} over the period of 1 h, using 1 M LiTFSI in DOL-DME as the electrolyte. Voltage *vs* time for (a) bismuth protected lithium anode, (b) arsenic protected lithium anode.

Another important conclusion that can be drawn from **Figure 23a-c** is the fact that alloy-protected lithium metal exhibits a lower average over-potential compared to lithium itself (65 *vs.* 90 mV), indicating better charge transport through the alloy protective layer compared to the native SEI formed on lithium metal. The effectiveness of the thin protective layer in stabilizing the lithium metal surface was further evaluated by impedance measurements in symmetric cells, as shown in **Figure 26**. Lithium is well known to undergo side reactions with the electrolyte[58], resulting in the progressive formation of an SEI/

passivation layer with poor ion conductivity that leads to ever-increasing charge transfer resistance on cycling, as shown in **Figure 26a**. In contrast, the protected lithium metal is significantly stabilized. The resistance remains almost constant over the cycling period (**Figure 26b**), suggesting the alloy surface protection layer is more resistant to reaction with the electrolyte. The much lower interfacial resistance implies favorable charge transfer/ atom diffusivity in the alloy layer, in consistent with the lower polarization observed in **Figure 23**.

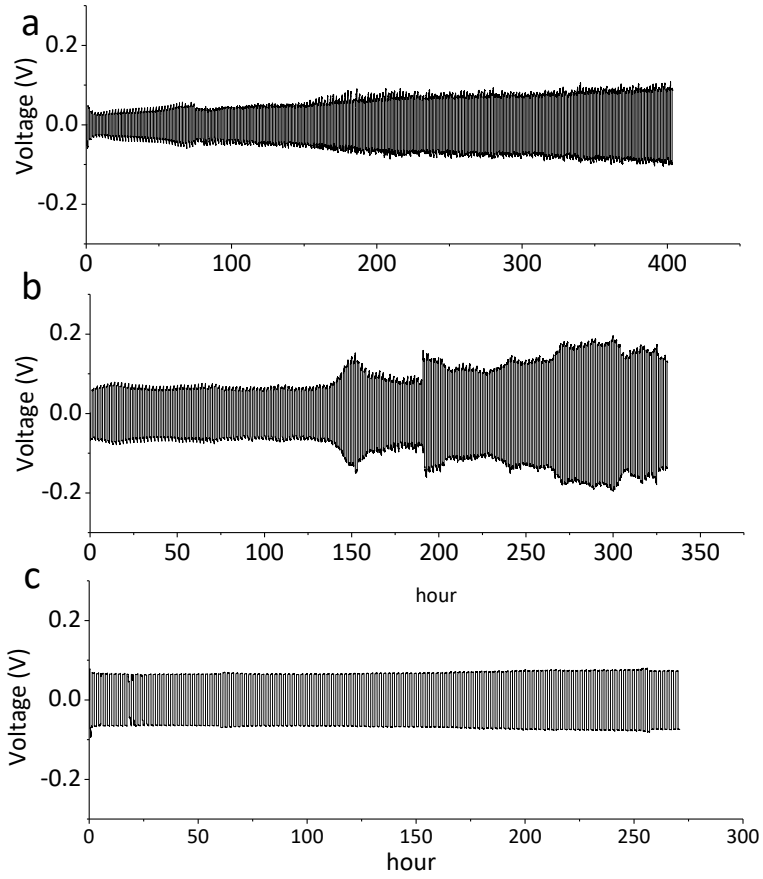

Figure 25. Lithium stripping/plating in symmetric cells at a current density of 2 mA cm^{-2} for 1 hour, using 1 M $LiPF_6$ in EC-DMC as the electrolyte. Voltage profile of (a) zinc protected lithium anode, (b) arsenic protected lithium anode, (c) indium protected lithium anode

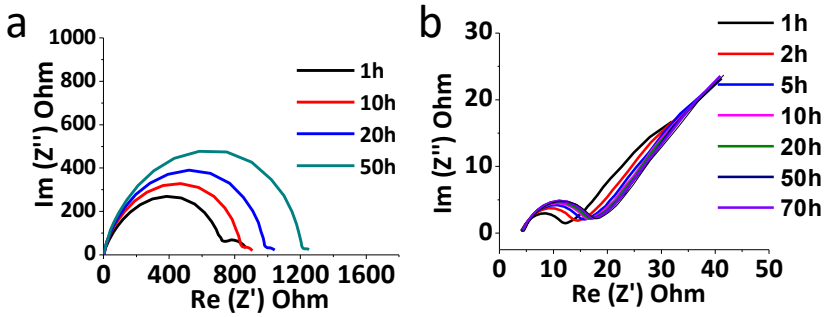

Figure 26. EIS analysis comparison of symmetric cells, (a) lithium anode, (b) indium protected lithium anode.

The performance of the alloy protected lithium served as an anode was further investigated in a full cell using $Li_4Ti_5O_{12}$ (LTO) as the cathode (**Figure 27**). LTO is a zero-strain electrode material that exhibits very high cycling stability even at high rates.[59] Therefore, any change in the cell's performance can be attributed to the anode. Cells were examined at a high rate of 5C, corresponding to a current density of 2.5 mA cm^{-2}. The discharge capacity of the cell with the lithium anode decreased gradually, becoming unstable and ultimately failing after 600 cycles. The cells with the protected lithium anode show remarkable cycling capability, however. Under the same cycling conditions, the cell with indium alloy protected lithium delivered stable capacity for 1500 cycles without significant fading (**Figure 27a**). In the cell with non-protected lithium anode, the overall overpotential increased on cycling and became significant after 100 cycles (**Figure 27b**), which is attributed to increasingly severe passivation/pulverization of the lithium surface during cycling as discussed in **Figure 19**. At the same time, the discharge capacity decreased gradually, becoming unstable and ultimately failing after 600 cycles. On the contrary, the

cells with the protected lithium anode show flat charge/discharge profile with no obvious overpotential increase (**Figure 27c,d**). This again supports that the alloys are able to protect the lithium metal from dendrite formation and passivation, providing a lithium metal anode with prolonged life.

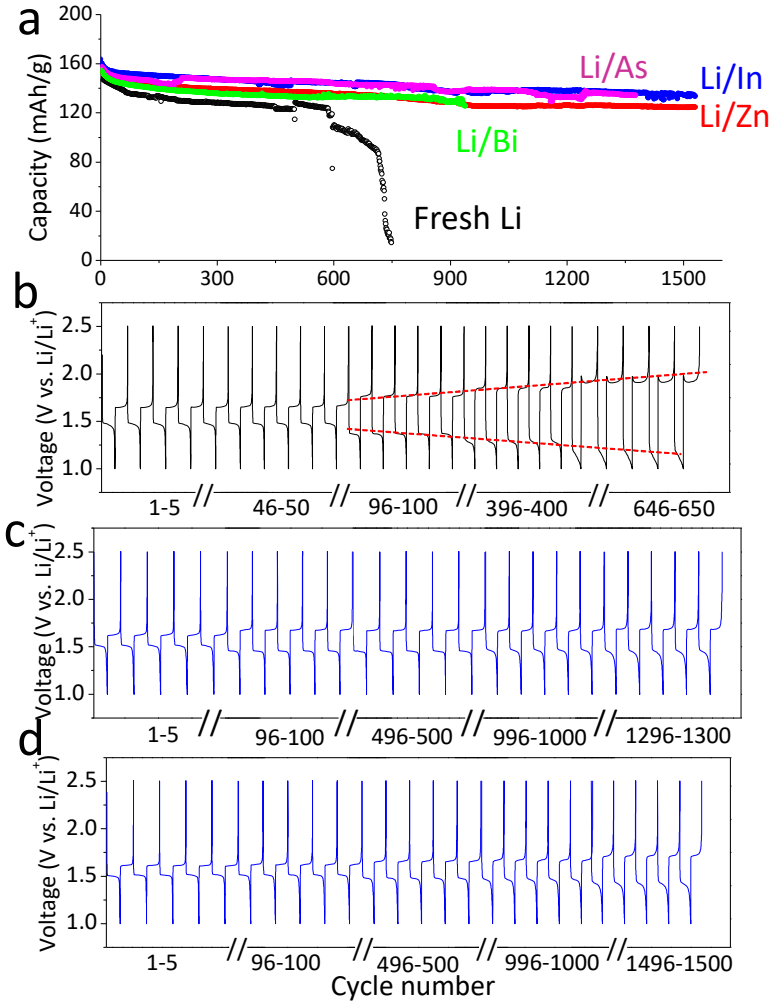

Figure 27. Electrochemical performance of the protected lithium metal. (a) Cycling performance of LTO electrodes paired with various lithium anodes. Voltage profiles of the LTO cells during cycling, (b) with fresh Li metal anode, (c) with an arsenic protected lithium anode, (d) with an indium protected lithium anode, (d). The areal loading of the LTO electrodes was about 3 mg cm^{-2}, and cells were tested at a 5C rate.

4.3 Conclusion

We have demonstrated that protecting lithium metal with Li-based surface alloys (Li-In, Li-Zn, Li-As and Li-Bi) provides much more stable interfaces after lithium electrodeposition. These alloys were prepared by a metathesis reaction in solution followed by self-alloying, enabling the suppression of dendrite growth effectively for repeated lithium stripping/plating deposition over 1400 hours at a practical current density of 2 mA/cm^2. All the characterizations and the significantly improved cycling performance are consistent with the results from our DFT calculations. Ultra-long cycling life was realized by those alloy-protected lithium metal anodes paired with a LTO cathode.

Conclusions and Future Perspectives

The work presented in this thesis includes a DFT-based computational study on the surface diffusion of lithium on different lithium alloys, predicting that the low diffusion barrier on those alloy make those alloys promising candidates for protecting lithium metal anode from dendrite formation. It was then followed by experimental validations which demonstrate that the surface property of lithium metal can be modified by those surface alloys and significant improvement in the cell performance was achieved with these alloy-protected lithium metal anodes.

In the first part of the thesis, our DFT calculations indicate that these lithium-rich alloys provide much lower energy barrier for surface diffusion of lithium, which theoretically lead to a novel approach to tackle the dendrite formation problem of lithium anode by surface alloying. Due to the much lower energy barriers on those surface alloys, lithium adatom can easily diffuse around the surface thus leading to an epitaxial growth behaviour. A smooth lithium electrodeposition morphology is predicted for lithium metal protected by these alloys, instead of growing dendrites on the surface.

In the second part of the thesis, we have confirmed that protecting lithium metal with Li-based surface alloys (Li-In, Li-Zn, Li-As and Li-Bi) provides much more stable interfaces for lithium electrodeposition than using the pure Li metal directly. These alloys were prepared by a metathesis reaction in solution followed by self-alloying, enabling the suppression of dendrite growth for repeated lithium stripping/plating deposition over 1400 hours at a practical current density of 2 mA/cm^2. Ultra-long cycling life was realized by those alloy-protected lithium metal anodes paired with a LTO cathode.

Our finding is significantly important in the battery field since it provides a simple and inexpensive strategy to stabilize the lithium metal anode, which fundamentally change its electrodeposition behaviour from dendrite preference to non-dendrite behaviour. It also shed light on a new and promising research field where lithium metal anode can be protected by applying surface layer with lower diffusion energy barrier. Given the existence of numerous available lithium alloys and the rich chemistry of surface science, combining with computational approaches, lithium metal batteries could certainly be commercialized in the future. Attention should be paid to these inexpensive metals such as zinc, which will have a huge potential to facilitate the large scale commercialization of lithium metal batteries. The same strategy can also be applied to sodium metal which suffers from the dendrite formation as well. This is under exploration in our laboratory.

Bibliography

1. Yoshino, A. *et al.* United States Patent: 4668595 - Secondary battery. (1987).
2. Armand, M. & Tarascon, J.-M. Building better batteries. *Nature* **451,** 652–657 (2008).
3. Bruce, P. G., Freunberger, S. A., Hardwick, L. J. & Tarascon, J.-M. Li-O2 and Li-S batteries with high energy storage. *Nat. Mater.* **11,** 19–29 (2012).
4. Xu, W. *et al.* Lithium metal anodes for rechargeable batteries. *Energy Environ. Sci.* **7,** 513–537 (2014).
5. Tarascon, J.-M. & Armand, M. Issues and challenges facing rechargeable lithium batteries. *Nature* **414,** 359–367 (2001).
6. Harry, K. J., Hallinan, D. T., Parkinson, D. Y., MacDowell, A. A. & Balsara, N. P. Detection of subsurface structures underneath dendrites formed on cycled lithium metal electrodes. *Nat. Mater.* **13,** 69–73 (2014).
7. Qian, J. *et al.* High rate and stable cycling of lithium metal anode. *Nat. Commun.* **6,** 6362 (2015).
8. Gofer, Y., Ben-Zion, M. & Aurbach, D. Solutions of LiAsF6 in 1,3-dioxolane for secondary lithium batteries. *J. Power Sources* **39,** 163–178 (1992).
9. Lu, Y., Tu, Z. & Archer, L. A. Stable lithium electrodeposition in liquid and nanoporous solid electrolytes. *Nat. Mater.* **13,** 961–969 (2014).
10. Bucur, C. B., Lita, A., Osada, N. & Muldoon, J. A soft, multilayered lithium–electrolyte interface. *Energy Environ. Sci.* **9,** 112–116 (2016).
11. Zheng, G. *et al.* Interconnected hollow carbon nanospheres for stable lithium metal anodes. *Nat. Nanotechnol.* **9,** 618–623 (2014).

12. Kozen, A. C. *et al.* Next-Generation Lithium Metal Anode Engineering via Atomic Layer Deposition. *ACS Nano* **9,** 5884–5892 (2015).
13. Marchioni, F. *et al.* Protection of lithium metal surfaces using chlorosilanes. *Langmuir ACS J. Surf. Colloids* **23,** 11597–11602 (2007).
14. Umeda, G. A. *et al.* Protection of lithium metal surfaces using tetraethoxysilane. *J. Mater. Chem.* **21,** 1593–1599 (2011).
15. Ding, F. *et al.* Dendrite-free lithium deposition via self-healing electrostatic shield mechanism. *J. Am. Chem. Soc.* **135,** 4450–4456 (2013).
16. Yang, C.-P., Yin, Y.-X., Zhang, S.-F., Li, N.-W. & Guo, Y.-G. Accommodating lithium into 3D current collectors with a submicron skeleton towards long-life lithium metal anodes. *Nat. Commun.* **6,** (2015).
17. Zhang, R. *et al.* Conductive Nanostructured Scaffolds Render Low Local Current Density to Inhibit Lithium Dendrite Growth. *Adv. Mater.* **28,** 2155–2162 (2016).
18. Armand, M. B., Duclot, M. J. & Rigaud, P. Polymer solid electrolytes: Stability domain. *Solid State Ion.* **3,** 429–430 (1981).
19. Li, Y., Fedkiw, P. S. & Khan, S. A. Lithium/V6O13 cells using silica nanoparticle-based composite electrolyte. *Electrochimica Acta* **47,** 3853–3861 (2002).
20. Khurana, R., Schaefer, J. L., Archer, L. A. & Coates, G. W. Suppression of lithium dendrite growth using cross-linked polyethylene/poly(ethylene oxide) electrolytes: a new approach for practical lithium-metal polymer batteries. *J. Am. Chem. Soc.* **136,** 7395–7402 (2014).

21. Rosso, M. *et al.* Dendrite short-circuit and fuse effect on Li/polymer/Li cells. *Electrochimica Acta* **51,** 5334–5340 (2006).
22. Monroe, C. & Newman, J. Dendrite Growth in Lithium/Polymer Systems A Propagation Model for Liquid Electrolytes under Galvanostatic Conditions. *J. Electrochem. Soc.* **150,** A1377–A1384 (2003).
23. Teyssot, A. *et al.* Inter-electrode in situ concentration cartography in lithium/polymer electrolyte/lithium cells. *J. Electroanal. Chem.* **584,** 70–74 (2005).
24. Zhao, Q. S., NuLi, Y. N., Guo, Y. S., Yang, J. & Wang, J. L. Reversibility of electrochemical magnesium deposition from tetrahydrofuran solutions containing pyrrolidinyl magnesium halide. *Electrochimica Acta* **56,** 6530–6535 (2011).
25. Jäckle, M. & Groß, A. Microscopic properties of lithium, sodium, and magnesium battery anode materials related to possible dendrite growth. *J. Chem. Phys.* **141,** 174710 (2014).
26. Ozhabes, Y., Gunceler, D. & Arias, T. A. Stability and surface diffusion at lithium-electrolyte interphases with connections to dendrite suppression. *ArXiv150405799 Cond-Mat Physicsphysics* (2015).
27. Jain, A. *et al.* Commentary: The Materials Project: A materials genome approach to accelerating materials innovation. *APL Mater.* **1,** 11002 (2013).
28. Qu, X. *et al.* The Electrolyte Genome project: A big data approach in battery materials discovery. *Comput. Mater. Sci.* **103,** 56–67 (2015).

29. Liu, M. *et al.* Spinel compounds as multivalent battery cathodes: a systematic evaluation based on ab initio calculations. *Energy Environ. Sci.* **8,** 964–974 (2015).
30. Bhatt, M. D. & O'Dwyer, C. Recent progress in theoretical and computational investigations of Li-ion battery materials and electrolytes. *Phys. Chem. Chem. Phys.* **17,** 4799–4844 (2015).
31. Nishijima, M. *et al.* Accelerated discovery of cathode materials with prolonged cycle life for lithium-ion battery. *Nat. Commun.* **5,** (2014).
32. Simon, C. M. *et al.* The materials genome in action: identifying the performance limits for methane storage. *Energy Environ. Sci.* **8,** 1190–1199 (2015).
33. Kresse, G. & Furthmüller, J. Efficient iterative schemes for ab initio total-energy calculations using a plane-wave basis set. *Phys. Rev. B* **54,** 11169–11186 (1996).
34. Kresse, G. & Furthmüller, J. Efficiency of ab-initio total energy calculations for metals and semiconductors using a plane-wave basis set. *Comput. Mater. Sci.* **6,** 15–50 (1996).
35. Henkelman, G., Uberuaga, B. P. & Jónsson, H. A climbing image nudged elastic band method for finding saddle points and minimum energy paths. *J. Chem. Phys.* **113,** 9901–9904 (2000).
36. Henkelman, G. & Jónsson, H. Improved tangent estimate in the nudged elastic band method for finding minimum energy paths and saddle points. *J. Chem. Phys.* **113,** 9978–9985 (2000).
37. Henkelman, G., Jóhannesson, G. & Jónsson, H. in *Theoretical Methods in Condensed Phase Chemistry* (ed. Schwartz, S. D.) 269–302 (Springer Netherlands, 2002).

38. Perdew, J. P., Burke, K. & Ernzerhof, M. Generalized Gradient Approximation Made Simple. *Phys. Rev. Lett.* **77,** 3865–3868 (1996).
39. Blöchl, P. E. Projector augmented-wave method. *Phys. Rev. B* **50,** 17953–17979 (1994).
40. Kresse, G. & Joubert, D. From ultrasoft pseudopotentials to the projector augmented-wave method. *Phys. Rev. B* **59,** 1758–1775 (1999).
41. Hull, A. W. The crystal structures of the common elements. *J. Frankl. Inst.* **193,** 189–216 (1922).
42. Doll, K., Harrison, N. M. & Saunders, V. R. A density functional study of lithium bulk and surfaces. *J. Phys. Condens. Matter* **11,** 5007 (1999).
43. Hosmani, S., Kuppusami, P. & Goyal, R. K. *An Introduction to Surface Alloying of Metals*. (Springer Science & Business, 2014).
44. Songster, J. & Pelton, A. D. The As-Li (arsenic-lithium) system. *J. Phase Equilibria* **14,** 238–239 (1993).
45. Sangster, J. & Pelton, A. D. The Bi-Li (Bismuth-Lithium) system. *J. Phase Equilibria* **12,** 447–450 (1991).
46. Pelton, A. D. The Li-Zn (Lithium-Zinc) System. *J. Phase Equilibria* **12,** 42–45 (1991).
47. Songster, J. & Pelton, A. D. The In-Li (Indium-Lithium) System. *J. Phase Equilibria* **12,** 37–41 (1991).
48. v. Benda, K. & Juza, R. Über ternäre Phasen im System Lithium–Kupfer–Arsen. *Z. Für Anorg. Allg. Chem.* **371,** 172–192 (1969).

49. Zintl, E. & Brauer, G. Konstitution der Lithium-Wismut-Legierungen: 14. Mitteilung über Metalle u. Legierungen. *Z. Für Elektrochem. Angew. Phys. Chem.* **41,** 297–303 (1935).

50. Zintl, E. & Schneider, A. Röntgenanalyse der Lithium-Zink-Legierungen (15. Mitteilung über Metalle und Legierungen). *Z. Für Elektrochem. Angew. Phys. Chem.* **41,** 764–767 (1935).

51. Stöhr, J., Müller, W. & Schäfer, H. Darstellung und Kristallstruktur von Li2In und Li13In3 / Preparation and Crystal Structure of Li2ln and Li13ln3. *Z. Für Naturforschung B* **33,** 1434–1437 (1978).

52. Richardson, T. J. & Chen, G. Solid solution lithium alloy cermet anodes. *J. Power Sources* **174,** 810–812 (2007).

53. Stark, J. K., Ding, Y. & Kohl, P. A. Dendrite-Free Electrodeposition and Reoxidation of Lithium-Sodium Alloy for Metal-Anode Battery. *J. Electrochem. Soc.* **158,** A1100–A1105 (2011).

54. Webb, S. A., Baggetto, L., Bridges, C. A. & Veith, G. M. The electrochemical reactions of pure indium with Li and Na: Anomalous electrolyte decomposition, benefits of FEC additive, phase transitions and electrode performance. *J. Power Sources* **248,** 1105–1117 (2014).

55. Hewitt, R. W. & Winograd, N. Oxidation of polycrystalline indium studied by x-ray photoelectron spectroscopy and static secondary ion mass spectroscopy. *J. Appl. Phys.* **51,** 2620–2624 (1980).

56. Kanamura, K., Tamura, H., Shiraishi, S. & Takehara, Z. XPS Analysis of Lithium Surfaces Following Immersion in Various Solvents Containing LiBF4. *J. Electrochem. Soc.* **142,** 340–347 (1995).
57. Zhou, W. *et al.* Plating a Dendrite-Free Lithium Anode with a Polymer/Ceramic/Polymer Sandwich Electrolyte. *J. Am. Chem. Soc.* **138,** 9385–9388 (2016).
58. Aurbach, D., Zinigrad, E., Cohen, Y. & Teller, H. A short review of failure mechanisms of lithium metal and lithiated graphite anodes in liquid electrolyte solutions. *Solid State Ion.* **148,** 405–416 (2002).
59. Ohzuku, T., Ueda, A. & Yamamoto, N. Zero-Strain Insertion Material of Li [Li1 / 3Ti5 / 3] O 4 for Rechargeable Lithium Cells. *J. Electrochem. Soc.* **142,** 1431–1435 (1995).